

Cordierite under hydrostatic compression: Anomalous elastic behavior as a precursor for a pressure-induced phase transition

RONALD MILETICH^{1,*}, G. DIEGO GATTA², THOMAS WILLI^{3,†}, PETER W. MIRWALD⁴, PAOLO LOTTI², MARCO MERLINI², NICOLA ROTIROTI² AND THOMAS LOERTING⁵

¹Institut für Mineralogie und Kristallographie, Universität Wien, Althanstrasse 14, A-1090 Wien, Austria

²Dipartimento di Scienze della Terra, Università degli Studi di Milano, Via Botticelli 23, I-20133 Milano, Italy

³Institut für Geowissenschaften, Universität Heidelberg, Im Neuenheimer Feld 234-236, D-69120 Heidelberg, Germany

⁴Institut für Mineralogie und Petrographie, Universität Innsbruck, Innrain 52, A-6020 Innsbruck, Austria

⁵Institut für Physikalische Chemie, Universität Innsbruck, Innrain 52, A-6020 Innsbruck, Austria

ABSTRACT

The high-pressure behavior of cordierite was investigated by means of in situ experiments using piston-cylinder press and diamond-anvil cell. Static compression in diamond-anvil cells was conducted with various penetrating and non-penetrating pressure media (H₂O up to 2 GPa, argon and 4:1-methanol-ethanol up to 7 GPa). The measurement of lattice parameters revealed neither a significant influence on the elasticity nor any indication for effects in analogy to over-hydration within the experimental pressure ranges. Volumetric compression experiments at constant rates up to 1.2 GPa in a piston-cylinder apparatus insinuate subtle irregularities in the low-pressure range at around ~0.35 and ~0.85 GPa. The $\Delta V/V$ contribution related to the anomalous compression behavior in that pressure range is of the order of 5×10^{-4} . The results obtained from single-crystal X-ray diffraction between 10⁻⁴ and 7 GPa revealed an unexpected and anomalous linear volume decrease, corresponding to $K_{T,298} = 131 \pm 1$ GPa for the bulk modulus and $K' = -0.4 \pm 0.3$ for its pressure derivative for a third-order Birch-Murnaghan equation of state. The compressional behavior of the main axis directions is anisotropic with $\beta_a^{-1} \approx \beta_b^{-1} > \beta_c^{-1}$ for an initial pressure regime up to ~3 GPa. At pressures above ~4 GPa, the compression of the *a*- and *b*-axis starts to differ significantly, with the *b*-axis showing elastic softening as indicated by negative values for $\partial(\beta_b^{-1})/\partial P$. The diversification between the *a*- and *b*-axis is also expressed by the pressure-depending increase of the distortion parameter Δ . The pronounced elastic softening in both the *b*-axis and *c*-axis directions $\partial(\beta_b^{-1})/\partial P = -4.3 \pm 0.9$, $\partial(\beta_c^{-1})/\partial P = -1.2 \pm 0.8$ are responsible for the apparent linear bulk compression, which indicates the structural instability and precedes a so far not reported ferroelastic phase transition to a triclinic polymorph, following a primitive lattice above the critical transition at ~6.9 GPa.

Keywords: Cordierite, high pressure, compressibility, elastic softening, phase transition

INTRODUCTION

The mineral physics and structure-property relationships of the silicate mineral cordierite, corresponding to (Mg,Fe)₂Al₄Si₅O₁₈ in a simplified form, has received considerable attention for various outstanding physical properties. The eminent properties of cordierite include the pronounced stability at high temperatures and the remarkable robust thermal shock resistance. The ability to sustain large temperature gradients and temperature changes on a short timescale is the consequence of relatively low thermal expansion (Hochella et al. 1979; Mirwald 1981; Ikawa et al. 1986; Camerucci et al. 2001). Another prominent aspect of the thermodynamic properties is related to the polymorphism at high temperatures (Miyashiro 1957; Langer and Schreyer 1969). The associated order/disorder phase transition, which

originates from the Al,Si distribution within the aluminosilicate (Al,Si)₆O₁₈ subunits, is accompanied by a symmetry change from orthorhombic (*Cccm*) to hexagonal (*P6/mcc*) symmetry above the critical temperature of ~1750 K (Meagher and Gibbs 1977; Putnis 1980a; Armbruster 1985a; Redfern et al. 1989; Daniels et al. 1994; Malcherek et al. 2001). Apart from the Al,Si ordering on tetrahedral sites and the mechanism of the transformation, numerous investigations focused on the structural origins of optical absorption properties, in particular on the remarkable macroscopic pleochroism in crystals. This includes the Fe²⁺,Fe³⁺ distribution (Faye et al. 1968; Goldman and Rossmann 1977; Abs-Wurmbach et al. 1989; Geiger et al. 2000a, 2000b; Khomenko et al. 2001) and, most recently, the radiocoloration and changes of the optical properties induced by irradiation (Vance and Price 1984; Nasdala et al. 2006; Weikusat et al. 2008, 2010; Miletich et al. 2010). In addition to the complex crystal chemistry, the microporous nature of the framework structure reveals the possibility for structural storage of a variable amount of extra-framework atoms (Na⁺, K⁺, Ca²⁺) and molecules, such as of H₂O,

* E-mail: ronald.miletich-pawliczek@univie.ac.at

† Present address: Institut für Geowissenschaften, Goethe Universität, Altenhöferallee 1, D-60438 Frankfurt a.M., Germany

CO₂, Ar, or N₂ (Bulbak et al. 2002; Cohen et al. 1977; Medenbach et al. 1980; Armbruster and Bloss 1980, 1982; Armbruster 1985b, 1986; Vry et al. 1990). This provides a high flexibility of the structure for substitutions according to $\text{C}^{\text{h}}(\text{Na}^+, \text{K}^+)_{m+n} \{^{6}[(\text{Mg}, \text{Fe}^{2+}, \text{Mn}^{2+})_{2-m} \text{Li}^+]^{4}[(\text{Al}, \text{Fe}^{3+})_{4-n} \text{Be}^{2+}]^{4} \text{Si}_5 \text{O}_{18}\} \cdot (\text{H}_2\text{O})_{\leq 2} (\text{CO}_2)_{\leq 0.5}$ stoichiometries (Bertoldi et al. 2004).

The majority of experimental studies are devoted to property changes related to the crystal chemistry and/or variations with temperature, in particular involving high temperatures. Investigations on cordierite at high-pressure conditions originated from the need to understand thermodynamic stability conditions, but are limited to only a few individual experimental studies (Mirwald and Maresch 1980; Mirwald 1982; Mirwald et al. 1984; Koepke and Schulz 1986). Most recently, Likhacheva et al. (2011, 2013) performed static compression on polycrystalline cordierite in aqueous media and describe a discontinuity in the volume properties in the pressure range between 4 and 5 GPa together with changes of the pressure-induced shifts of Raman modes above 4.7 GPa. Both experimental observations have been attributed to pressure-induced over-hydration by excess H₂O contents (Likhacheva et al. 2013). Potential structural changes assigned to the extra-framework channel content have also been presumed to be responsible for small volume discontinuities as observed on isothermal compression and decompression in piston-cylinder apparatus (PCA). Mirwald and Maresch (1980) and Mirwald (1982) described two discontinuities, which are supposed to occur at ~0.22 and ~0.90 GPa with $\Delta V/V$ discontinuities of about -0.05 to -0.3 vol% in volumetric measurements. Diffraction studies on single crystals in diamond-anvil cells later supported only the subtle discontinuity at 0.90±0.06 GPa, claiming unusual low compressibility for the pressure interval below. It is noteworthy to mention that no structural changes were observed. In addition, the possible influence of the type of pressure medium was suggested, by interaction with the structure through the open pores (Mirwald et al. 1984; Koepke and Schulz 1986). Nevertheless, the restricted number of data points, their scattering and the uncertainties of individual data points are somewhat too large with respect to the reported small volume changes, and leave some certain doubt about the significance of the existence of transitions related to structural changes. The determination of the coefficients of the elastic tensor and measurements of elastic moduli (Toohill et al. 1999; Bubeck 2009) complement the view on elasticity from static compression studies. Most recent results provide even a picture of the temperature dependency of the elastic properties at 1 bar (Haussühl et al. 2011).

Compared to the earlier experimental investigations, both the PCA and DAC high-pressure techniques have significantly improved and, in addition, single-crystal techniques can be expected to reveal much better constraints on subtle effects. The purpose of the present study is to re-investigate the static elasticity and to compare the compressional behavior in various nominally penetrating and non-penetrating pressure media [according to Gatta (2008)] under hydrostatic conditions. This includes compression of a large single-crystal sample in a PCA but also that of single-crystal samples in DACs. One focus of these investigations is to tackle the earlier proposed discontinuities and to extend the investigated pressure range. High-pressure structure investigations were carried out to monitor the structural evolution related

to the possible interpenetration of molecular species from the pressure medium into the open framework structure. The required accuracy is achieved by employing state-of-the-art single-crystal X-ray diffraction (XRD) techniques, with a sufficient density of data points across the critical pressure regions to determine high-resolution equations of states (EoSs) within the hydrostatic limits of uniform pressure conditions.

MATERIALS AND METHODS

Sample material and oriented crystal specimen

Single-crystal samples used in this study correspond to the sample material from Madagascar with oriented crystal specimen of homogeneous sodium-poor Na_{0.03}[(Mg_{1.78}Fe_{0.25})Al_{3.98}Si_{4.99}O₁₈](H₂O)_{0.45}(CO₂)_{0.07} (sample Tsi1) and Na_{0.03}[(Mg_{1.90}Fe_{0.12})Al_{3.99}Si_{4.98}O₁₈](H₂O)_{0.54}(CO₂)_{0.04} (sample Tsi2) according to Miletich et al. (2010). The Fe/(Mg+Fe) composition of individual crystal specimen was checked by energy-dispersive X-ray analyses on using a scanning-electron microscope. Crystal orientation was provided by means of polarized microscopy and conventional X-ray oscillation photographs. Double-sided polished crystal platelets, ~40 to 70 μm thick, were prepared from thin sections parallel (*hk0*), (001)-, and (010)-plane directions (corresponding to the sample notations “Tsi1”, “Tsi2_b,” and “Tsi2_c”). The (*hk0*) section of Tsi1 approximates a crystallographic (810)-plane direction. Several cylindrically shaped flat disks (120 to 220 μm in diameter) were prepared using a microdrill device as described by Förtisch et al. (1992). For the piston-cylinder experiments a non-oriented 1.889 g cylinder (diameter: 9.60 mm; height: 7.06 mm) was drilled out from a crystal specimen from Soto, Argentina {composition: Na_{0.004}[(Mg_{1.23}Fe_{0.74}Mn_{0.05})Al_{4.02}Si_{4.95}O₁₈](H₂O)_{0.41}(CO₂)_{0.08}; Schreyer et al. (1979); Mirwald et al. (1984)}.

Static compression measurements in DACs

All high-pressure loadings were carried out using ETH-type DAC with Be backing plates and steel gaskets (stainless steel, material type 1.4310, pre-indented from initial 250 μm to the starting thickness given in Table 1). Crystal specimen equilibrated in air, without additional treatment prior to loading, were pressurized at room temperature using either liquid water, cryogenically liquefied argon, or a water-free (4:1)-methanol-ethanol mixture acting as hydrostatic pressure medium. Pressures were adjusted by means of laser-induced fluorescence following the ruby scale (Mao et al. 1986). Precise pressure values were derived from the V/V_0 ratio of the unit-cell volumes of quartz (Angel et al. 1997) as determined from a synthetic SiO₂ standard crystal. All lattice parameters were measured with customized Huber 5042 four-circle diffractometers using non-monochromatized Mo-radiation. The setting angles of diffracted Bragg peaks were recorded with a point detector, using motorized slits (2 × 6 mm), employing the method of eight-position diffracted-beam centering (King and Finger 1979), and using the fitting routines as implemented in the SINGLE software (Angel and Finger 2011). The results of symmetry-constrained vector least-squares refinements for five different series of individual high-pressure loadings (series A and B in H₂O, series C and D in argon, series E in methanol-ethanol mix) are listed in Table 2.

Additional data points, in particular at pressures above the observed transition, were collected on beamline ID09A at the European Synchrotron Radiation Facility (ESRF, Grenoble) using the synchrotron X-ray beam from an undulator source. The horizontally and vertically focused beam, being monochromatized at ~30 keV ($\lambda = 0.414384 \text{ \AA}$), gives an almost parallel beam of ~30 × 30 μm² on the sample. Tiny hand-selected crystal fragments were pressurized in membrane-type DACs with Boehler-Almax anvils of 0.6 mm culet size. Measurements were performed with the DAC being mounted on a ω -rotation goniometer collecting 1° frames in the ±30 rotation range, recording all diffraction patterns with the Mar 555 flat-panel detector (fixed 2 $\theta = 0^\circ$ at a distance of 310 mm from the sample). Single-crystal sample images were finally processed with the CrysAlis software (Agilent 2012) using more than 700 observed reflections.

Volumetric experiments with a piston-cylinder apparatus

The volumetric measurements at ambient temperature (298 K) were conducted with an electronically controlled piston-cylinder apparatus using a steel vessel with a 10 mm bore (Salzmann et al. 2006). The sample was enveloped in 2.28 g Pb-foil and accommodated inside the bore of the steel vessel. The pressure-change rate of the isothermal compression runs was 31 MPa/min. Pressure, piston displacement (pd) as a measure of volume change (V) and temperature are simultaneously

TABLE 1. Details of the high-pressure DAC loadings (pressure range, pressure-chamber dimensions) and of the individual crystal specimen (crystal material, orientation, dimensions)

HP-measurement	DAC type/backing plates/anvils ^a	<i>P</i> range (GPa)	Crystal (μm)	Orientation (μm)	Dimensions	Pressure chamber
EoS in H ₂ O (series A)	ETH/polyBe/sbc, C = 0.6 mm	0.07–0.21	Tsi1#1	disk//(<i>hk</i> 0)	$\varnothing = 155, H = 45$	$\varnothing = 230, H = 75$
EoS in H ₂ O (series B)	ETH/polyBe/sbc, C = 0.6 mm	0.06–2.01	Tsi1#1 ^b	disk//(<i>hk</i> 0)	$\varnothing = 155, H = 45$	$\varnothing = 235, H = 85$
EoS in Ar (series C)	ETH/polyBe/sbc, C = 0.6 mm	1.28–6.44	Tsi2_b#1	plate//(<i>0</i> 10)	$210 \times 100 \times 65$	$\varnothing = 250, H = 115$
EoS in Ar (series D)	ETH/polyBe/sbc, C = 0.6 mm	0.89–4.67	Tsi2_b#2	plate//(<i>0</i> 10)	$165 \times 80 \times 65$	$\varnothing = 250, H = 95$
EoS in M-E (series E)	ETH/polyBe/sbc, C = 0.6 mm	1.05–6.61	Tsi1# ^a	disk//(<i>hk</i> 0)	$\varnothing = 155, H = 45$	$\varnothing = 250, H = 105$
P>P _c (series F and G)	mDAC/—/BA, C = 0.6 mm	>7.0	Tsi2_c ^c	plate//(<i>0</i> 01)	$30 \times 30 \times 10$	$\varnothing = 250, H = 80$
Structure in H ₂ O	ETH/diaBP/sbc, C = 0.6 mm	0.39–1.75	Tsi2_b#3	plate//(<i>0</i> 10)	$160 \times 140 \times 60$	$\varnothing = 300, H = 120$
Structure in M-E	ETH/polyBe/sbc, C = 0.6 mm	1.07–6.98	Tsi1#2	disk//(<i>hk</i> 0)	$\varnothing = 195, H = 50$	$\varnothing = 300, H = 120$

^a Abbreviations: “ETH” = ETH diamond-anvil cell, “mDAC” = membrane-type diamond-anvil cell, “polyBe” = polycrystalline beryllium backing plate, “diaBP” = Sinter-crystal UP7020 diamond backing plate, “sbc” = standard brilliant-cut diamond anvil, “BA” = Böhler-Almax diamond anvil, “C” = unbevelled culet-face diameter.

^b Same crystal as used for series A.

^c Several micro-size crystal fragments from Tsi2_c used for synchrotron XRD.

TABLE 2. Lattice parameters, unit-cell volumes, and calculated distortion parameter Δ of cordierite in air and at pressurized in water, argon, and 4:1 methanol-ethanol mixture

No.	V-Qz (\AA^3)	<i>P</i> (GPa)	<i>a</i> (\AA)	<i>b</i> (\AA)	<i>c</i> (\AA)	<i>V</i> (\AA^3)	Δ (°)	No.	V-Qz (\AA^3)	<i>P</i> (GPa)	<i>a</i> (\AA)	<i>b</i> (\AA)	<i>c</i> (\AA)	<i>V</i> (\AA^3)	Δ (°)
Cordierite in air															
A00 ^a	–	0.0001	17.0719(4)	9.7224(3)	9.3489(2)	1551.74(6)	0.2540	B36	109.325(12)	1.383(6)	17.0204(5)	9.6939(4)	9.3090(3)	1535.93(8)	0.2517
B00 ^a	–	0.0001	17.0721(8)	9.7211(8)	9.3496(8)	1551.66(14)	0.2567	B37	109.108(20)	1.473(10)	17.0160(6)	9.6914(4)	9.3061(4)	1534.66(9)	0.2516
C00 ^a	–	0.0001	17.0738(8)	9.7193(8)	9.3451(8)	1550.78(15)	0.2619	B38	108.814(19)	1.598(9)	17.0112(8)	9.6886(5)	9.3029(5)	1533.24(12)	0.2517
Cordierite in water															
B43 ^{b,d}	113.048(16)	0.0001	17.0717(9)	9.7230(6)	9.3493(6)	1551.87(16)	0.2527	B39	108.645(17)	1.670(8)	17.0076(6)	9.6863(4)	9.3002(3)	1532.12(9)	0.2521
B16	112.888(33)	0.060(16)	17.0710(6)	9.7239(4)	9.3457(4)	1551.35(9)	0.2502	B40	108.435(19)	1.761(9)	17.0055(10)	9.6854(6)	9.2976(6)	1531.36(15)	0.2515
A02	112.874(19)	0.065(14)	17.0710(6)	9.7233(4)	9.3462(3)	1551.34(9)	0.2513	B41	108.149(22)	1.887(11)	17.0002(7)	9.6823(5)	9.2943(4)	1529.84(11)	0.2516
B04	112.872(20)	0.066(10)	17.0715(6)	9.7232(5)	9.3457(4)	1551.29(10)	0.2521	B42	107.863(40)	2.013(20)	16.9955(10)	9.6800(6)	9.2915(6)	1528.60(16)	0.2508
B03	112.868(20)	0.067(10)	17.0715(5)	9.7233(4)	9.3457(3)	1551.30(8)	0.2519	Cordierite in argon							
B07	112.770(20)	0.100(10)	17.0701(6)	9.7222(4)	9.3448(3)	1550.85(9)	0.2524	D05 ^{e*}	–	0.0001	17.0727(5)	9.7200(4)	9.3436(4)	1550.54(10)	0.2594
B05	112.753(23)	0.105(12)	17.0694(5)	9.7227(3)	9.3449(3)	1550.89(8)	0.2507	D01	110.546(25)	0.889(12)	17.0318(6)	9.7006(13)	9.3188(8)	1539.64(25)	0.2515
B08	112.709(33)	0.120(16)	17.0688(5)	9.7215(3)	9.3445(3)	1550.58(7)	0.2523	C01	109.502(22)	1.275(9)	17.0123(8)	9.6877(17)	9.3085(8)	1534.13(31)	0.2546
A03	112.650(22)	0.140(11)	17.0680(5)	9.7212(4)	9.3439(3)	1550.35(8)	0.2520	C02	108.123(38)	1.860(17)	16.9886(7)	9.6769(18)	9.2923(9)	1527.62(32)	0.2491
B06	112.592(31)	0.160(15)	17.0671(5)	9.7211(4)	9.3432(3)	1550.15(9)	0.2512	D02	107.432(18)	2.212(9)	16.9773(6)	9.6699(11)	9.2833(7)	1524.02(22)	0.2500
B02	112.499(23)	0.191(11)	17.0667(5)	9.7214(3)	9.3419(3)	1549.94(8)	0.2502	D03	105.216(25)	3.330(12)	16.9344(7)	9.6436(11)	9.2559(7)	1511.58(23)	0.2529
B17	112.499(22)	0.191(11)	17.0668(6)	9.7204(4)	9.3423(4)	1549.85(10)	0.2522	C03	104.496(25)	3.658(14)	16.9201(6)	9.6343(14)	9.2421(7)	1506.58(26)	0.2549
B01	112.475(22)	0.199(11)	17.0659(7)	9.7204(5)	9.3421(4)	1549.74(10)	0.2513	C04	103.729(19)	4.092(11)	16.9073(10)	9.6276(21)	9.2324(11)	1502.83(38)	0.2536
A01	112.448(19)	0.209(9)	17.0661(5)	9.7202(3)	9.3420(3)	1549.70(7)	0.2519	D04	102.923(28)	4.674(14)	16.8846(8)	9.6088(11)	9.2146(7)	1494.99(24)	0.2644
B10	112.421(41)	0.218(20)	17.0656(5)	9.7199(4)	9.3415(3)	1549.53(8)	0.2519	C05	101.267(32)	5.630(22)	16.8538(10)	9.5821(22)	9.1872(10)	1483.69(39)	0.2813
B15	112.417(27)	0.219(13)	17.0647(7)	9.7195(5)	9.3417(4)	1549.42(11)	0.2517	C06	100.107(45)	6.439(32)	16.8277(15)	9.5597(36)	9.1633(16)	1474.08(61)	0.2952
B18	112.380(22)	0.232(11)	17.0646(5)	9.7188(4)	9.3418(3)	1549.31(8)	0.2528	Cordierite in 4:1 methanol-ethanol mix							
B09	112.376(22)	0.233(11)	17.0638(5)	9.7188(4)	9.3415(3)	1549.19(8)	0.2520	E09 ^{b,f}	112.994(12)	0.0001	17.0716(7)	9.7234(10)	9.3494(6)	1551.94(17)	0.2518
B14	112.336(27)	0.247(13)	17.0641(3)	9.7186(3)	9.3414(3)	1549.17(8)	0.2527	G00	–	0.0001	17.0930(6)	9.7289(4)	9.347(5)	1554.4(8)	0.2648
B13	112.296(27)	0.261(13)	17.0631(5)	9.7188(4)	9.3402(3)	1548.91(8)	0.2512	E01	110.071(16)	1.052(6)	17.0246(6)	9.7008(11)	9.3224(6)	1539.61(20)	0.2432
B12	112.227(24)	0.284(12)	17.0621(5)	9.7176(4)	9.3395(3)	1548.51(8)	0.2524	E08	109.081(15)	1.454(6)	17.0087(5)	9.6912(8)	9.3111(7)	1534.79(15)	0.2440
B11	112.087(32)	0.333(16)	17.0602(5)	9.7167(4)	9.3385(3)	1548.04(8)	0.2520	E02	108.242(19)	1.813(9)	16.9933(6)	9.6835(9)	9.3010(6)	1530.53(18)	0.2418
B19	111.931(26)	0.388(13)	17.0600(7)	9.7166(5)	9.3376(4)	1547.84(11)	0.2520	E07	105.646(17)	3.050(8)	16.9441(7)	9.6536(14)	9.2686(7)	1516.08(23)	0.2446
B20	111.640(27)	0.491(13)	17.0543(5)	9.7135(3)	9.3339(3)	1546.22(8)	0.2516	E03	103.909(18)	3.994(9)	16.9081(7)	9.6234(10)	9.2473(6)	1504.66(17)	0.2625
B22	111.590(44)	0.509(22)	17.0535(14)	9.7130(9)	9.3339(8)	1546.08(23)	0.2517	E06	102.465(14)	4.859(7)	16.8784(7)	9.6022(10)	9.2225(7)	1494.69(18)	0.2701
B23	111.432(20)	0.566(10)	17.0523(6)	9.7119(4)	9.3316(4)	1545.42(10)	0.2525	E04	101.753(20)	5.549(10)	16.8551(8)	9.5832(11)	9.2041(7)	1486.70(24)	0.2806
B24	111.268(27)	0.626(13)	17.0491(6)	9.7101(4)	9.3302(3)	1544.60(9)	0.2524	G01	–	5.73(2) ^c	16.9025(5)	9.6209(3)	9.175(3)	1492.0(5)	0.2610
B25	111.051(22)	0.706(11)	17.0462(5)	9.7088(5)	9.3279(4)	1543.75(10)	0.2517	E05	99.876(13)	6.613(7)	16.8229(9)	9.5590(13)	9.1648(9)	1473.79(28)	0.2913
B21	111.004(26)	0.724(13)	17.0450(6)	9.7084(4)	9.3273(3)	1543.48(9)	0.2511	G02	–	7.84(2) ^c	15.566(2)	9.625(4)	9.085(5)		
B26	110.667(15)	0.851(8)	17.0426(7)	9.7062(5)	9.3239(4)	1542.35(10)	0.2526				$\alpha =$	$\beta =$	$\gamma =$	1357.5(1.1)	n.d.
B28	110.632(20)	0.864(10)	17.0415(7)	9.7059(5)	9.3228(4)	1542.01(11)	0.2520				90.36(4) ^e	85.90(2) ^e	89.16(2) ^e		
B29	110.587(48)	0.881(24)	17.0379(6)	9.7044(4)	9.3231(3)	1541.52(8)	0.2509	F01	–	9.0(1) ^c	15.496(7)	9.574(3)	9.0377(16)		
B30	110.476(25)	0.924(12)	17.0377(5)	9.7035(4)	9.3217(3)	1541.11(9)	0.2524				$\alpha =$	$\beta =$	$\gamma =$	1337.4(8)	n.d.
B27	110.443(33)	0.937(17)	17.0363(6)	9.7034(4)	9.3211(3)	1540.88(9)	0.2511				90.02(2) ^e	85.99(2) ^e	88.90(3) ^e		
B31	110.150(27)	1.051(13)	17.0330(5)	9.7010(3)	9.3178(3)	1539.64(7)	0.2520	<i>Note:</i> Distortion parameter $\Delta = 1.094 (a - \sqrt{3}b)$, Selkreg and Bloss (1980).							
B32	109.975(17)	1.120(8)	17.0295(6)	9.6990(4)	9.3160(3)	1538.71(9)	0.2520	^a At 1 bar, crystal mounted on glass fiber.							
B33	109.896(17)	1.150(8)	17.0282(5)	9.6988(3)	9.3150(3)	1538.40(7)	0.2509	^b At 1 bar, crystal mounted in DAC without pressure medium.							
B34	109.744(14)	1.212(7)	17.0266(5)	9.6970(4)	9.3139(3)	1537.78(8)	0.2526	^c Pressure determined by ruby fluorescence method.							
B35	109.641(17)	1.254(8)	17.0240(5)	9.6960(3)	9.3125(3)	1537.15(7)	0.2517	^d After compression in H ₂ O.							
								^e After compression in argon.							
								^f After compression in ethanol-methanol.							

recorded in 0.5 s intervals during the experiment. Besides a controlling inspection of the piston displacement vs. pressure loop, the data analysis mainly relies on a difference technique developed from differential pressure analysis (Mirwald and Massonne 1980; Mirwald 2005a, 2005b, 2008) where the changes in piston displacement (Δp) per a chosen time interval (Δt ; e.g., 15 s) are used as parameters (cf. Fig. 1). The difference quotient of $\Delta p/\Delta t$ as a parameter of the compression behavior represents a qualitative (dV/dP) compressibility coefficient. While the reading resolution of pressure is at 10^{-6} GPa due to the electronic recording technique, its relevant precision is at 5×10^{-5} GPa. The accuracy of the pressure

determination is estimated to be within 50 MPa. The reading resolution of the piston displacement (Δp_d), the second crucial parameter is at 10^{-5} mm, the relevant precision is 5×10^{-4} mm. Since the piston displacement measurements are of relative nature, the precision of (Δp_d) allows the tracing of volume changes in the range of 5×10^{-2} mm. This corresponds to a volume change of 0.02 mm³, thus providing a precision in (V/V) in the order of 10^{-4} for our 706 mm³ cordierite sample. The low compression and decompression rates and the use of lead as a soft pressure-transmitting material keeps the friction at about 20 MPa, which implies a subordinate role in the pressure determination.

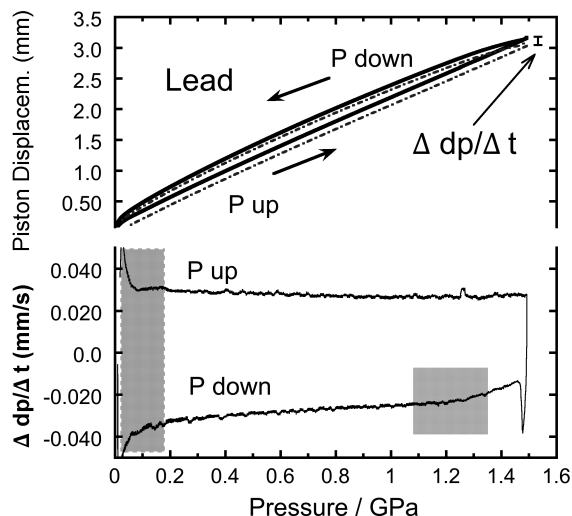


FIGURE 1. Compression experiment of lead up to 1.5 GPa as calibration reference for the performed compression experiments on cordierite. Top: the solid line gives the loop (piston displacement vs. pressure) obtained from compression (P up) - decompression (P down) run. The adjacent loop (dotted-dashed line) represents the dp - P -loop displaced by Δt (usually 15 s, here for better presentation $\Delta t = 200$ s). Bottom: the $\Delta dp/\Delta t$ -parameter plotted vs. pressure. The hatched areas indicate regions of strong influences by the characteristics of the high-pressure apparatus (apparatus function).

Data collection and structure refinements at 1 bar

Both sample crystals used for the high-pressure structure investigations were examined prior to loading into the pressure cell by performing a full structure refinement at ambient pressure (air) from the samples being mounted on glass fibers. X-ray intensity data collections were performed using an Xcalibur-Oxford Diffraction diffractometer with instrument specifications as listed in Table 3. To maximize data coverage and redundancy, a combination of ω and ϕ scans was chosen. Integrated intensities were corrected for Lorentz-polarization (L_p) and for absorption effects (analytical absorption corrections by Gaussian integration based upon the physical description of the crystal) using the CrysAlis software package (Agilent 2012). The structure refinement using anisotropic displacement parameters was performed with the SHELX-97 program (Sheldrick 1997), starting from the atomic coordinates of Miletich et al. (2010), and using neutral atomic scattering factors for Si, Al, Mg, Fe, and O from the *International Tables of Crystallography* (Wilson and Prince 1999). A full Si/Al-ordering was confirmed at the tetrahedral sites (i.e., T₁1, T₁6, T₂1, T₂3, T₂6). A mixed scattering curve of Mg and Fe was used to model the octahedral M site, but this did not lead to a significant fraction of Fe, and so the scattering curve of Mg alone was used in the last cycles of the refinement. Two extra-framework sites (here labeled as Ch1 1/4 and Ch2 1/4) as found in the difference-Fourier map were assigned using the scattering curve of oxygen as being potentially occupied by H₂O, and a further one (labeled as Na) following reported site allocations (e.g., Miletich et al. 2010). All extra-framework sites were modeled with isotropic displacement regime. Data pertaining to the XRD intensity data collection are listed in Table 3 (CIF¹ is available), resulting site coordinates, occupancy and displacement parameters are listed in Table 4, bond distances and other structure parameters are given in Table 5.

XRD intensity data collection at pressures <7 GPa

An ETH-type DAC was used for all high-pressure intensity data collections using anvils with $C = 0.6$ mm. Loading of the sample in H₂O was performed in a DAC

with a low-background assembly using synthetic type-Ib single-crystal diamond backing plates (Miletich et al. 2000, 2005; Krauss et al. 2005; Periotto et al. 2011). The sample pressurized in methanol-ethanol mix, was loaded in a DAC equipped with standard Be-backing plates. Spherical standard rubies (Chervin et al. 2002) served as optical pressure sensors. The four intensity data collections of the sample in H₂O at 0.39(6), 1.41(8), and 1.75(5) GPa, including one measurement in the DAC at 1 bar without pressure medium, were performed with a *KUMA*-diffractometer using the scan settings reported in Table 3. Integrated intensity data up to $2\theta_{\max} \sim 70^\circ$ were corrected for L_p and absorption effects using the ABSORB6.0 program (Angel 2004). The empirical absorption corrections for the sample crystal and the DAC components was carried out in agreement with the correction applied by Hejny et al. (2012). The seven intensity data sets of the sample in methanol-ethanol mix were collected between 10^{-4} GPa (with the crystal in the DAC without any pressure medium) and 6.98(5) GPa (Table 3). Data collections were performed with the same Xcalibur-Oxford Diffraction diffractometer used for the measurements at 1 bar, based on the equivalent data collection strategy, but with an exposure time of 60 s/frame. The refinements were performed with the SHELX-97 program (Sheldrick 1997), starting from the structure model refined at room- P (with the crystal in air) and using isotropic displacement parameters. Only one channel site (i.e., Ch1 1/4), was successfully located for the sample in methanol-ethanol mix, while the Fourier summations yielded no significant electron densities for any channel site in the sample pressurized in H₂O (Tables 4a and 4b). Site coordinates, occupancies, and displacement parameters pertaining to the refinements are listed in Table 4; bond distances and other structure parameters are listed in Table 5.

RESULTS AND DISCUSSION

Volume compression measurements in piston-cylinder pressure apparatus

Since Mirwald et al. (1984) reported a discontinuous compression behavior at pressures below 1 GPa, we re-examined that pressure range by piston-cylinder compression experiments with the aim to provide a better volumetric resolution due to the very improved data acquisition technique. Because of the qualitative character of the volumetric technique, calibration experiments have been conducted with Pb and NaCl, both well-studied materials (Birch 1966). The continuous monitoring of compression provides: (1) a good survey on the pressure characteristic of the apparatus ("apparatus function"), and (2) allows the detection of even very small changes in the compression behavior relative to volume discontinuities or to compression anomalies of materials to be investigated.

Figure 1 shows, as a calibration example, a compression-decompression run on Pb up to 1.5 GPa. The piston displacement vs. pressure loop (Fig. 1, top) shows the typical behavior, i.e., in the low-pressure range up to 0.2 GPa the loop is strongly influenced by the stress-strain characteristic of the vessel plus the sample set up. The upstroke and downstroke track of Pb show a smooth course without any irregularity, apart from a slight kink on the beginning of the down stroke, which reflects the termination of the stress-strain reversal of vessel-sample set up. This situation is also reflected by the difference parameter $\Delta dp/\Delta t$ when plotted vs. pressure (Fig. 1, bottom). This difference parameter is obtained by slight displacement of the pressure loop equivalent to a time interval of usually 15 s. This appears in the plot of piston displacement vs. pressure in Figure 1 (top) as a slightly displaced second loop. The $\Delta dp/\Delta t$ track of the calibration run on lead is very smooth. Only at low pressure and on the down stroke side of the pressure loop, the above-mentioned features related to the apparatus function are noticed. The compression-decompression results on NaCl, the second material used for calibration, are similar.

In Figure 2, the $\Delta dp/\Delta t$ tracks (upstroke and downstroke) for

¹ Deposit item AM-14-214, CIF. Deposit items are stored on the MSA web site and available via the American Mineralogist Table of Contents. Find the article in the table of contents at GSW (aminin.geoscienceworld.org) or MSA (www.minsocam.org), and then click on the deposit link.

TABLE 3. Data pertaining to the XRD intensity data collections and structure refinement of cordierite compressed in different media

Medium	Crystal Tsi2_b#							
	air ^a	air ^b	H ₂ O	H ₂ O	H ₂ O			
Pressure (GPa)	10 ⁻⁴	10 ⁻⁴	0.39(6)	1.41(8)	1.75(5)			
<i>a</i> (Å)	17.089(2)	17.094(2)	17.082(3)	17.029(3)	17.021(3)			
<i>b</i> (Å)	9.733(1)	9.691(7)	9.689(7)	9.662(7)	9.659(8)			
<i>c</i> (Å)	9.361(1)	9.360(3)	9.346(3)	9.322(3)	9.306(3)			
max. 2θ (°)	69.6	69.3	68.5	68.4	69.3			
(sinθ/λ) _{max} (Å ⁻¹)	0.8030	0.8000	0.7919	0.7909	0.8000			
Detector, scan type	CCD, ω/φ	PD, ω	PD, ω	PD, ω	PD, ω			
Scan width (°)	0.5	1.2	1.2	1.2	1.2			
Scan speed (°/s)	–	0.02	0.02	0.02	0.02			
Exposure time (s)	–	20	–	–	–			
No. refls.	16112	3162	3215	3171	2951			
No. unique refls.	1597	300	259	307	288			
with <i>F</i> _o > 4σ(<i>F</i> _o)	1222	229	251	235	217			
No. parameter	96	27	27	27	27			
<i>R</i> _{int}	0.050	0.083	0.087	0.082	0.084			
<i>R</i> ₁ , <i>F</i> _o > 4σ(<i>F</i> _o)	0.042	0.082	0.092	0.089	0.109			
<i>wR</i> ²	0.052	0.116	0.133	0.138	0.141			
Goof	1.092	1.427	1.329	1.412	1.541			
δ <i>e</i> _{max} (Å ⁻³)	+0.40	+0.62	+0.69	+1.03	+0.68			
δ <i>e</i> _{min} (Å ⁻³)	-0.39	-0.67	-0.86	-0.88	-0.89			
Medium	Crystal Tsi1#2							
	air ^a	air ^b	4:1 M-E	4:1 M-E	4:1 M-E	4:1 M-E	4:1 M-E	4:1 M-E
Pressure (GPa)	10 ⁻⁴	10 ⁻⁴	1.07(5)	2.31(5)	3.80(5)	5.20(5)	6.40(5)	6.98(5)
<i>a</i> (Å)	17.060(6)	17.098(16)	17.020(20)	16.973(13)	16.938(14)	16.890(15)	16.842(19)	16.840(16)
<i>b</i> (Å)	9.716(3)	9.698(4)	9.668(7)	9.657(7)	9.652(4)	9.622(4)	9.602(5)	9.583(4)
<i>c</i> (Å)	9.352(2)	9.354(5)	9.294(4)	9.285(5)	9.261(3)	9.215(4)	9.204(3)	9.179(3)
max. 2θ (°)	72.7	78.6	77.9	78.5	78.2	78.2	76.4	78.2
(sinθ/λ) _{max} (Å ⁻¹)	0.8340	0.8912	0.8845	0.8902	0.8844	0.8844	–	–
Detector, scan type	CCD, ω/φ	CCD, ω/φ	CCD, ω/φ	CCD, ω/φ				
Scan width (°)	0.5	0.5	0.5	0.5	0.5	0.5	0.5	0.5
Scan speed (°/s)	–	–	–	–	–	–	–	–
Exposure time (s)	20	60	60	60	60	60	60	60
No. refls.	16497	2675	2313	2342	2282	2254	2341	1998
No. unique refls.	1625	718	710	689	688	655	653	636
with <i>F</i> _o > 4σ(<i>F</i> _o)	1294	292	264	264	263	246	242	212
No. parameter	83	30	30	30	30	30	30	30
<i>R</i> _{int}	0.0364	0.0569	0.0497	0.0630	0.0578	0.0549	0.0522	0.0546
<i>R</i> ₁ , <i>F</i> _o > 4σ(<i>F</i> _o)	0.0678	0.0690	0.0928	0.0648	0.0801	0.0702	0.0960	0.0708
<i>wR</i> ²	0.0553	0.0779	0.1041	0.0798	0.0902	0.0881	0.0872	0.0758
Goof	1.445	1.052	1.121	1.415	1.091	1.122	1.021	1.187
δ <i>e</i> _{max} (Å ⁻³)	+0.74	+0.52	+0.73	+0.55	+0.46	+0.46	+0.62	+1.80
δ <i>e</i> _{min} (Å ⁻³)	-0.62	-0.82	-1.12	-0.61	-0.81	-0.56	-0.78	-0.72

Notes: Space group: *Cc*cm. $R_{int} = \sum |F_{obs}^2 - F_{obs}^2(\text{mean})| / \sum F_{obs}^2$; $R_1 = \sum (|F_{obs}| - |F_{calc}|) / \sum F_{obs}$; $wR_2 = \{ \sum [w(F_{obs}^2 - F_{calc}^2)]^2 / \sum [w(F_{obs}^2)] \}^{0.5}$, $w = 1 / [\sigma^2(F_{obs}^2) + (0.02 \cdot P)^2]$, $P = [\text{Max}(F_{obs}^2) + 2 \cdot F_{calc}^2] / 3$.

^a Crystal mounted on glass fiber.

^b Crystal in DAC.

the investigated cordierite sample are given. The related loop of piston displacement (*dp*) vs. pressure loop (Fig. 1, top) appears smooth. However, the inspection of the $\Delta dp / \Delta t$ -tracks reveals two irregularities in the compression behavior of cordierite, at 0.36 and at 0.75 GPa on compression, and at 0.75 and 0.33 GPa on decompression. Instead of a smooth, slightly curved course as indicated in the plot by a curved line serving as a guide to the eye, the experimental data of the compression track shows a sort of bump between the two pressures, while the decompression track exhibits an almost linear behavior in that pressure interval. The two $\Delta dp / \Delta t$ -discontinuities on the compression and decompression track show no clear hysteresis. Since the *dp* vs. *P* tracks show no discrete volume change, the two irregularities are interpreted as a slight change in compressibility of cordierite. Based on a very detailed evaluation of the compression stroke of the *dp*-*P*-loop, the deviations in volume were calculated inferring a linear compression behavior in this pressure interval. The $\Delta V / V$ obtained is in the order of 5×10^{-4} . This suggests a subtle compression irregularity, which is contained by two compressibility

anomalies. The implication for the overall compression behavior of cordierite is small as demonstrated in Figure 3. Considering the given experimental precision, a more quantitative analysis of these volumetric data are therefore limited. Nevertheless, the analytical findings re-confirm in principle the occurrence of subtle irregularities in the compression behavior in a similar fashion as reported by Mirwald et al. (1984).

The volumetric data obtained in the PCA experiments give again evidence of this phenomenon due to the fact to represent a continuous volumetric record on compression and decompression. Despite all improvements of experimental techniques, including pressure corrections, the data obtained here suggest subtle irregularities in the compressibility, but no evident volume discontinuity. The specific volume *dV/V* change attributed to the anomalous compression behavior between 0.35 and 0.85 GPa lies in the order of 5×10^{-4} . Considering the circumstances that the PCA experiments were performed under water-free conditions, one can exclude to a certain extent the influence of external fluid to control the compression behavior of cordierite.

TABLE 4a. Atomic fractional coordinates and displacement parameters (\AA^2) of cordierite compressed in 4:1 methanol-ethanol (M-E)

Site	x/a	y/b	z/c	$U_{\text{iso}}/U_{\text{eq}}$	Site	x/a	y/b	z/c	$U_{\text{iso}}/U_{\text{eq}}$
10⁻⁴ GPa (in air)									
M	0.16258(5)	1/2	1/4	0.0067(2)	T ₂ 3	-0.1335(3)	0.2370(3)	0	0.0132(4)
T ₁	1/4	1/4	0.25012(8)	0.0066(2)	T ₂ 6	0.0518(3)	0.3070(3)	0	0.0132(4)
T ₁ 6	0	1/2	1/4	0.0058(2)	O ₁	0.2482(3)	0.1024(4)	0.1412(3)	0.0145(7)
T ₂ 1	0.19258(4)	0.07797(8)	0	0.0056(2)	O ₁ 6	0.0623(3)	0.4173(4)	0.1507(4)	0.0145(7)
T ₂ 3	-0.13523(4)	0.23725(8)	0	0.0055(2)	O ₂	-0.1727(3)	0.3109(4)	0.1419(4)	0.0145(7)
T ₂ 6	0.05084(5)	0.30791(9)	0	0.0056(2)	O ₂ 6	-0.0416(4)	0.2433(7)	0	0.0145(7)
O ₁	0.24739(7)	0.10315(13)	0.14106(12)	0.0081(3)	O ₂ 1	0.1221(4)	0.1831(6)	0	0.0145(7)
O ₁ 6	0.06215(7)	0.41606(14)	0.15108(12)	0.0084(3)	O ₂ 3	-0.1665(6)	0.0804(5)	0	0.0145(7)
O ₂ 3	-0.17325(7)	0.30997(14)	0.14144(13)	0.0088(3)	Ch1 1/4	0.0397(16)	0	1/4	0.0145(7)
O ₂ 6	-0.04316(11)	0.24734(21)	0	0.0127(4)	5.20(5) GPa M-E				
O ₂ 1	0.12250(11)	0.18435(21)	0	0.0122(4)	M	0.1622(3)	1/2	1/4	0.0183(8)
O ₂ 3	-0.16462(11)	0.07967(20)	0	0.0118(4)	T ₁	1/4	1/4	0.2520(3)	0.0159(4)
Ch1 1/4	0.0591(18)	0	1/4	0.07(1)	T ₁ 6	0	1/2	1/4	0.0159(4)
Ch2 1/4	0	0	1/4	0.08(1)	T ₂ 1	0.1943(3)	0.0767(3)	0	0.0159(4)
10⁻⁴ GPa (in DAC)									
M	0.16247(19)	1/2	1/4	0.0107(7)	T ₂ 3	-0.1332(3)	0.2376(3)	0	0.0159(4)
T ₁	1/4	1/4	0.2504(3)	0.0105(4)	T ₂ 6	0.0515(3)	0.3066(3)	0	0.0159(4)
T ₁ 6	0	1/2	1/4	0.0105(4)	O ₁	0.2483(3)	0.1021(4)	0.1425(4)	0.0166(7)
T ₂ 1	0.19259(19)	0.07796(24)	0	0.0105(4)	O ₁ 6	0.0625(3)	0.4161(4)	0.1507(4)	0.0166(7)
T ₂ 3	-0.1345(2)	0.2371(3)	0	0.0105(4)	O ₂ 3	-0.1723(3)	0.3108(4)	0.1425(4)	0.0166(7)
T ₂ 6	0.0508(2)	0.3088(3)	0	0.0105(4)	O ₂ 6	-0.0410(4)	0.2404(7)	0	0.0166(7)
O ₁	0.2472(3)	0.1024(3)	0.1416(3)	0.0103(6)	O ₂ 1	0.1224(5)	0.1841(6)	0	0.0166(7)
O ₁ 6	0.0627(2)	0.4178(3)	0.1505(3)	0.0103(6)	O ₂ 3	-0.1657(6)	0.0807(6)	0	0.0166(7)
O ₂ 3	-0.1733(3)	0.3099(3)	0.1423(3)	0.0103(6)	Ch1 1/4	0.0412(17)	0	1/4	0.0166(7)
O ₂ 6	-0.0423(3)	0.2457(6)	0	0.0103(6)	6.40(5) GPa M-E				
O ₂ 1	0.1228(4)	0.1870(5)	0	0.0103(6)	M	0.1618(2)	1/2	1/4	0.0099(8)
O ₂ 3	-0.1641(5)	0.0793(5)	0	0.0103(6)	T ₁	1/4	1/4	0.2528(3)	0.0106(4)
Ch1 1/4	0.0359(14)	0	1/4	0.0103(6)	T ₁ 6	0	1/2	1/4	0.0106(4)
1.07(5) GPa M-E									
M	0.1613(3)	1/2	1/4	0.0139(9)	T ₂ 1	0.1952(3)	0.0766(3)	0	0.0106(4)
T ₁	1/4	1/4	0.2510(4)	0.0134(4)	T ₂ 3	-0.1332(3)	0.2371(3)	0	0.0106(4)
T ₁ 6	0	1/2	1/4	0.0134(4)	T ₂ 6	0.0524(3)	0.3061(3)	0	0.0106(4)
T ₂ 1	0.1931(3)	0.0769(3)	0	0.0134(4)	O ₁	0.2500(3)	0.1015(4)	0.1415(4)	0.0108(6)
T ₂ 3	-0.1346(3)	0.2377(3)	0	0.0134(4)	O ₁ 6	0.0638(3)	0.4174(4)	0.1506(3)	0.0108(6)
T ₂ 6	0.0520(3)	0.3069(3)	0	0.0134(4)	O ₂	-0.1714(3)	0.3124(4)	0.1426(4)	0.0108(6)
O ₁	0.2472(3)	0.1020(4)	0.1427(4)	0.0119(6)	O ₂ 6	-0.0409(4)	0.2375(7)	0	0.0108(6)
O ₁ 6	0.0619(3)	0.4164(5)	0.1498(4)	0.0119(6)	O ₂ 1	0.1236(5)	0.1833(7)	0	0.0108(6)
O ₂ 3	-0.1739(3)	0.3112(4)	0.1420(4)	0.0119(6)	O ₂ 3	-0.1663(6)	0.0815(6)	0	0.0108(6)
O ₂ 6	-0.0422(4)	0.2464(7)	0	0.0119(6)	Ch1 1/4	0.0355(16)	0	1/4	0.0108(6)
O ₂ 1	0.1241(5)	0.1858(7)	0	0.0119(6)	6.98(5) GPa M-E				
O ₂ 3	-0.1643(7)	0.0806(6)	0	0.0119(6)	M	0.1618(2)	1/2	1/4	0.0119(7)
Ch1 1/4	0.0400(19)	0	1/4	0.0119(6)	T ₁	1/4	1/4	0.2534(3)	0.0105(4)
2.31(5) GPa M-E									
M	0.16230(19)	1/2	1/4	0.0128(6)	T ₁ 6	0	1/2	1/4	0.0105(4)
T ₁	1/4	1/4	0.2513(3)	0.0114(3)	T ₂ 1	0.1948(3)	0.0758(3)	0	0.0105(4)
T ₁ 6	0	1/2	1/4	0.0114(3)	T ₂ 3	-0.1334(3)	0.2366(3)	0	0.0105(4)
T ₂ 1	0.1933(2)	0.0778(2)	0	0.0114(3)	T ₂ 6	0.0522(3)	0.3049(3)	0	0.0105(4)
T ₂ 3	-0.1343(2)	0.2370(3)	0	0.0114(3)	O ₁	0.2497(3)	0.1014(3)	0.1423(3)	0.0141(6)
T ₂ 6	0.0514(2)	0.3074(2)	0	0.0114(3)	O ₁ 6	0.0637(3)	0.4162(4)	0.1513(3)	0.0141(6)
O ₁	0.2475(3)	0.1025(3)	0.1418(3)	0.0102(5)	O ₂	-0.1720(3)	0.3128(3)	0.1418(4)	0.0141(6)
O ₁ 6	0.0622(3)	0.4163(3)	0.1503(3)	0.0102(5)	O ₂ 6	-0.0406(4)	0.2360(6)	0	0.0141(6)
O ₂ 3	-0.1729(3)	0.3100(3)	0.1428(3)	0.0102(5)	O ₂ 1	0.1240(4)	0.1827(6)	0	0.0141(6)
O ₂ 6	-0.0426(3)	0.2428(5)	0	0.0102(5)	O ₂ 3	-0.1687(6)	0.0830(5)	0	0.0141(6)
O ₂ 1	0.1223(4)	0.1848(5)	0	0.0102(5)	Ch1 1/4	0.0352(18)	0	1/4	0.0141(6)
O ₂ 3	-0.1655(5)	0.0805(4)	0	0.0102(5)	3.80(5) GPa M-E				
Ch1 1/4	0.0363(14)	0	1/4	0.0102(5)	M	0.1622(2)	1/2	1/4	0.0154(8)
3.80(5) GPa M-E									
M	0.1622(2)	1/2	1/4	0.0154(8)	T ₁	1/4	1/4	0.2526(3)	0.0132(4)
T ₁	1/4	1/4	0.2526(3)	0.0132(4)	T ₁ 6	0	1/2	1/4	0.0132(4)
T ₁ 6	0	1/2	1/4	0.0132(4)	T ₂ 1	0.1945(3)	0.0772(3)	0	0.0132(4)
T ₂ 1	0.1945(3)	0.0772(3)	0	0.0132(4)	Notes: The scattering curve of Mg was used to model the M site, and the refined site occupancy at 0.0001 GPa (in air, and then fixed at any pressure) was 12.72(8) e ⁻ ; the scattering curve of Al was used to model the T ₁ 1 and T ₂ 6 sites, assuming a full occupancy; the scattering curve of Si was used to model the T ₁ 6, T ₂ 1, and T ₂ 3 sites, assuming a full occupancy; the scattering curve of O was used to model the Ch1 1/4 [s.o.f. 1.14(9)e ⁻] and Ch2 1/4 [s.o.f. 2.2(2)e ⁻] sites. The Ch2 1/4 site was not detected at high-pressure conditions. The anisotropic displacement parameter at 0.0001 GPa (in air) are available in the CIF ¹ . For the HP structure refinements, the following constraints were applied:				

$U_{\text{iso}}(\text{T}_1) = U_{\text{iso}}(\text{T}_6) = U_{\text{iso}}(\text{T}_2) = U_{\text{iso}}(\text{T}_3) = U_{\text{iso}}(\text{T}_6) = U_{\text{iso}}(\text{T}_6)$ and $U_{\text{iso}}(\text{O}_1) = U_{\text{iso}}(\text{O}_6) = U_{\text{iso}}(\text{O}_3) = U_{\text{iso}}(\text{O}_2) = U_{\text{iso}}(\text{O}_2) = U_{\text{iso}}(\text{O}_2) = U_{\text{iso}}(\text{O}_2) = U_{\text{iso}}(\text{Ch1 1/4})$.

For compression at room temperature, the elastic behavior is similar to “dry” cordierite (Mirwald 1982), and interpenetration of molecular species from the pressurizing fluids apparently requires at low pressures additional high temperatures (Le Breton and Schreyer 1993).

Equations of state and the role of pressure media

The results of high-precision XRD measurements of the lattice parameters and unit-cell volumes on static compression are

summarized in Table 2. Compression data sets of single-crystal cordierite in the particular pressure media comprise various loadings of the same or equivalent sample crystals, i.e., series A and B in H₂O, and series C and D in Ar. Figure 4 shows the evolution of the three different *P-V* data sets according to the (quasi) hydrostatic compression in H₂O, argon, and methanol-ethanol pressure fluids. Compression in H₂O was achieved under true hydrostatic conditions in liquid water up to 0.9 GPa, followed by quasi-hydrostatic compression in soft ice-VI up to 2.1 GPa,

TABLE 4b. Atomic fractional coordinates and displacement parameters (\AA^2) of cordierite compressed in H_2O

Site	x/a	y/b	z/c	$U_{\text{iso}}/U_{\text{eq}}$	Site	x/a	y/b	z/c	$U_{\text{iso}}/U_{\text{eq}}$
10⁻⁴ GPa (in air)									
M	0.16255(4)	1/2	1/4	0.0075(2)	O ₂ 1	0.1223(5)	0.1846(13)	0	0.0058(11)
T ₁	1/4	1/4	0.25015(9)	0.0075(2)	O ₂ 3	-0.1651(6)	0.0792(9)	0	0.0058(11)
T ₁ 6	0	1/2	1/4	0.0068(3)	1.41(8) GPa H₂O				
T ₂ 1	0.19259(3)	0.07771(6)	0	0.0058(2)	M	0.1625(2)	1/2	1/4	0.0053(12)
T ₂ 3	-0.13517(3)	0.23739(6)	0	0.0061(2)	T ₁ 1	1/4	1/4	0.2506(7)	0.0056(6)
T ₂ 6	0.05094(4)	0.30813(7)	0	0.0088(2)	T ₁ 6	0	1/2	1/4	0.0056(6)
O ₁	0.24731(6)	0.10303(10)	0.14108(12)	0.0131(3)	T ₂ 1	0.1933(2)	0.0768(7)	0	0.0056(6)
O ₆	0.06229(6)	0.41632(11)	0.15122(12)	0.0129(3)	T ₂ 3	-0.1349(2)	0.2367(7)	0	0.0056(6)
O ₃	-0.17330(6)	0.31009(11)	0.14163(13)	0.0136(3)	O ₁	0.2471(4)	0.1025(8)	0.1420(8)	0.0076(11)
O ₆	-0.04314(8)	0.24833(17)	0	0.0174(4)	O ₆	0.0623(3)	0.4142(9)	0.1526(7)	0.0076(11)
O ₂ 1	0.12246(8)	0.18494(16)	0	0.0170(4)	O ₂ 1	-0.1735(3)	0.3101(7)	0.1401(6)	0.0076(11)
O ₂ 3	-0.16466(9)	0.07955(15)	0	0.0161(4)	O ₂ 3	-0.0419(4)	0.2446(16)	0	0.0076(11)
Ch1 1/4	-0.05980	0	1/4	0.11(1)	O ₂ 1	0.1235(5)	0.1858(12)	0	0.0076(11)
Ch2 1/4	0	0	1/4	0.07(1)	O ₂ 3	-0.1653(6)	0.0793(9)	0	0.0076(11)
Na	0	0	0	0.04(1)	1.75(5) GPa H₂O				
10⁻⁴ GPa (in DAC)									
M	0.16264(19)	1/2	1/4	0.0011(10)	M	0.1626(3)	1/2	1/4	0.0081(14)
T ₁	1/4	1/4	0.2500(6)	0.0044(5)	T ₁ 1	1/4	1/4	0.2496(7)	0.0073(7)
T ₁ 6	0	1/2	1/5	0.0044(5)	T ₁ 6	0	1/2	1/4	0.0073(7)
T ₂ 1	0.19240(19)	0.0776(7)	0	0.0044(5)	T ₂ 1	0.1931(3)	0.0773(8)	0	0.0073(7)
T ₂ 3	-0.1353(2)	0.2372(7)	0	0.0044(5)	T ₂ 3	-0.1346(3)	0.2368(8)	0	0.0073(7)
T ₂ 6	0.0510(2)	0.3086(7)	0	0.0044(5)	T ₂ 6	0.0512(3)	0.3065(8)	0	0.0073(7)
O ₁	0.2463(3)	0.1018(7)	0.1423(6)	0.0104(10)	O ₁	0.2471(4)	0.1023(9)	0.1417(7)	0.0091(13)
O ₆	0.0622(2)	0.4173(9)	0.1503(6)	0.0104(10)	O ₆	0.0622(3)	0.4139(11)	0.1522(9)	0.0091(13)
O ₃	-0.1734(3)	0.3087(7)	0.1430(6)	0.0104(10)	O ₃	-0.1729(4)	0.3075(8)	0.1424(7)	0.0091(13)
O ₆	-0.0434(4)	0.2484(15)	0	0.0104(10)	O ₆	-0.0424(5)	0.2464(20)	0	0.0091(13)
O ₂ 1	0.1225(4)	0.1853(11)	0	0.0104(10)	O ₂ 1	0.1234(6)	0.1858(14)	0	0.0091(13)
O ₂ 3	-0.1657(5)	0.0798(9)	0	0.0104(10)	O ₂ 3	-0.1660(7)	0.0805(11)	0	0.0091(13)
0.39(6) GPa H₂O									
M	0.1622(2)	1/2	1/4	0.0056(12)					
T ₁	1/4	1/4	0.2501(5)	0.0031(5)					
T ₁ 6	0	1/2	1/4	0.0031(5)					
T ₂ 1	0.1926(2)	0.0779(7)	0	0.0031(5)					
T ₂ 3	-0.1353(2)	0.2372(7)	0	0.0031(5)					
T ₂ 6	0.0507(2)	0.3081(7)	0	0.0031(5)					
O ₁	0.2471(4)	0.1023(8)	0.1413(6)	0.0058(11)					
O ₆	0.0623(3)	0.4159(9)	0.1512(7)	0.0058(11)					
O ₃	-0.1735(3)	0.3094(7)	0.1414(6)	0.0058(11)					
O ₆	-0.0427(4)	0.2444(16)	0	0.0058(11)					

Notes: The scattering curve of Mg was used to model the M site, and the refined site occupancy at 0.0001 GPa (in air, and then fixed at any pressure) was 12.00(4) e⁻; the scattering curve of Al was used to model the T₁ and T₂6 sites, assuming a full occupancy; the scattering curve of Si was used to model the T₁6, T₂1, and T₂3 sites, assuming a full occupancy; the scattering curve of O was used to model the Ch1 1/4 [s.o.f. 1.6(2)e⁻] and Ch2 1/4 [s.o.f. 2.2(3)e⁻] sites and that of sodium for the Na site [s.o.f. 0.45(7)e⁻]. All the channel sites were not detected with the crystal in the DAC. The anisotropic displacement parameter at 0.0001 GPa (in air) are available in the CIF. For the HP structure refinements, the following constraints were applied:

$U_{\text{iso}}(\text{T}_{1}) = U_{\text{iso}}(\text{T}_{6}) = U_{\text{iso}}(\text{T}_{2}1) = U_{\text{iso}}(\text{T}_{2}3) = U_{\text{iso}}(\text{T}_{2}6)$ and $U_{\text{iso}}(\text{O}_{1}) = U_{\text{iso}}(\text{O}_{6}) = U_{\text{iso}}(\text{O}_{3}) = U_{\text{iso}}(\text{O}_{2}6) = U_{\text{iso}}(\text{O}_{2}1) = U_{\text{iso}}(\text{O}_{2}3) = U_{\text{iso}}(\text{Ch1 } 1/4)$.

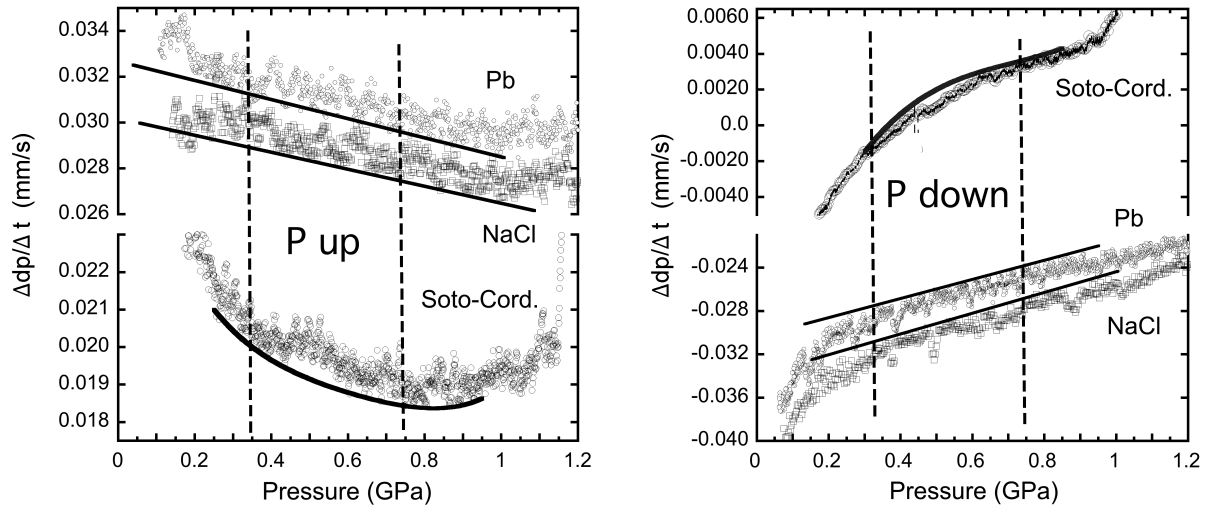


FIGURE 2. (left) The $\Delta dp/\Delta t$ parameter derived from a compression run of Soto cordierite plotted vs. pressure in comparison with $\Delta dp/\Delta t$ data obtained from calibration runs on lead and NaCl. (right) The equivalent data obtained on decompression. While the reference materials Pb and NaCl exhibit a linear behavior of the $\Delta dp/\Delta t$ -parameter, the Soto cordierite reveals in each track two subtle irregularities at around 0.3 and 0.75 GPa encompassing a deviation n from the general compression trend (line as a guide to the eye).

TABLE 5a. Selected bond distances (Å), ring “diameters” (Å), and other structural parameters of cordierite compressed in methanol-ethanol mix at different pressures

<i>P</i> (GPa)	0.0001	0.0001 ^a	1.07(5)	2.31(5)
M-O ₁ (×2)	2.098(2)	2.098(5)	2.095(7)	2.081(5)
M-O _{1,6} (×2)	2.111(2)	2.101(5)	2.093(7)	2.097(5)
M-O ₃ (×2)	2.115(2)	2.109(4)	2.094(4)	2.095(3)
<M-O>	2.108	2.103	2.094	2.091
T ₁ -O ₃ (×2)	1.756(2)	1.750(5)	1.737(6)	1.750(4)
T ₁ -O ₁ (×2)	1.754(2)	1.757(4)	1.751(5)	1.736(4)
<T ₁ -O>	1.755	1.754	1.744	1.743
T _{1,6} -O ₆ (×4)	1.626(2)	1.628(4)	1.622(5)	1.620(4)
T ₂ -O ₂	1.580(3)	1.594(7)	1.578(9)	1.587(7)
T ₂ -O ₃	1.604(3)	1.601(6)	1.599(8)	1.600(6)
T ₂ -O ₁ (×2)	1.635(2)	1.638(4)	1.633(6)	1.625(5)
<T ₂ -O>	1.614	1.618	1.611	1.609
T ₃ -O ₆	1.574(2)	1.577(8)	1.574(9)	1.557(7)
T ₃ -O ₃	1.611(3)	1.612(6)	1.601(8)	1.601(6)
T ₃ -O ₃ (×2)	1.634(2)	1.646(4)	1.642(5)	1.638(4)
<T ₃ -O>	1.613	1.620	1.615	1.609
T ₆ -O ₆	1.708(3)	1.706(7)	1.708(9)	1.714(7)
T ₆ -O ₂	1.713(3)	1.707(7)	1.695(9)	1.688(7)
T ₆ -O ₆ (×2)	1.771(2)	1.772(4)	1.757(5)	1.757(4)
<T ₆ -O>	1.741	1.739	1.729	1.729
O ₂ ↔ O ₃	5.826(3)	5.819(13)	5.806(18)	5.829(12)
O ₆ ↔ O ₆	5.026(3)	4.980(8)	4.976(10)	4.905(8)
O ₂ ↔ O ₂	5.504(3)	5.549(9)	5.545(12)	5.478(9)
ε ₁₀₀₁	0.904(1)	0.905(2)	0.906(3)	0.891(2)
T ₂ -O ₂ -T ₂	176.3(1)	177.7(4)	178.2(6)	176.2(4)
T ₃ -O ₃ -T ₃	179.2(1)	179.4(4)	179.4(5)	177.8(3)
T ₆ -O ₆ -T ₆	163.4(1)	162.0(4)	163.0(5)	160.6(4)
O ₆ -O ₃ -O ₂	112.5(1)	112.5(3)	112.8(3)	111.0(2)
O ₂ -O ₂ -O ₂	117.87(9)	116.7(3)	116.6(4)	117.2(3)
O ₂ -O ₆ -O ₂	129.62(9)	130.8(3)	130.7(4)	131.8(3)
V _{polMg}	11.77(2)	11.68(5)	11.53(6)	11.48(5)
ξ	0.0574	0.0576	0.0591	0.0586
<i>P</i> (GPa)	3.80(5)	5.20(5)	6.40(5)	6.98(5)
M-O ₁ (×2)	2.073(6)	2.057(6)	2.038(6)	2.035(6)
M-O _{1,6} (×2)	2.085(6)	2.079(6)	2.047(6)	2.047(6)
M-O ₃ (×2)	2.090(4)	2.079(4)	2.061(4)	2.058(4)
<M-O>	2.083	2.072	2.049	2.047
T ₁ -O ₃ (×2)	1.737(5)	1.735(5)	1.742(5)	1.735(5)
T ₁ -O ₁ (×2)	1.760(4)	1.745(5)	1.756(5)	1.752(4)
<T ₁ -O>	1.749	1.740	1.749	1.744
T _{1,6} -O ₆ (×4)	1.612(5)	1.613(5)	1.618(5)	1.618(5)
T ₂ -O ₂	1.596(8)	1.594(8)	1.582(8)	1.572(8)
T ₂ -O ₃	1.593(7)	1.589(7)	1.594(7)	1.584(7)
T ₂ -O ₁ (×2)	1.611(5)	1.618(5)	1.613(5)	1.619(5)
<T ₂ -O>	1.603	1.605	1.601	1.599
T ₃ -O ₆	1.558(9)	1.559(9)	1.554(8)	1.562(8)
T ₃ -O ₃	1.611(7)	1.606(7)	1.595(8)	1.587(7)
T ₃ -O ₃ (×2)	1.635(5)	1.630(5)	1.631(5)	1.628(5)
<T ₃ -O>	1.610	1.606	1.603	1.601
T ₆ -O ₆	1.698(9)	1.687(9)	1.705(8)	1.697(8)
T ₆ -O ₂	1.687(8)	1.680(8)	1.682(8)	1.684(8)
T ₆ -O ₆ (×2)	1.764(4)	1.753(5)	1.761(4)	1.762(4)
<T ₆ -O>	1.728	1.718	1.727	1.726
O ₂ ↔ O ₃	5.850(15)	5.809(15)	5.816(15)	5.897(15)
O ₆ ↔ O ₆	4.904(10)	4.829(8)	4.764(10)	4.725(8)
O ₂ ↔ O ₂	5.441(9)	5.445(9)	5.452(10)	5.453(10)
ε ₁₀₀₁	0.887(3)	0.878(3)	0.879(3)	0.875(3)
T ₂ -O ₂ -T ₂	174.7(5)	175.9(5)	175.8(5)	176.7(5)
T ₃ -O ₃ -T ₃	177.0(4)	177.7(5)	177.3(5)	174.2(4)
T ₆ -O ₆ -T ₆	161.0(5)	158.8(5)	157.4(5)	156.9(5)
O ₆ -O ₃ -O ₂	110.2(3)	110.1(3)	109.6(3)	107.8(3)
O ₂ -O ₂ -O ₂	118.3(3)	117.1(3)	116.4(3)	116.8(3)
O ₂ -O ₆ -O ₂	131.5(4)	132.8(4)	134.0(4)	135.3(4)
V _{polMg}	11.36(5)	11.17(5)	10.86(5)	10.81(5)
ξ	0.0567	0.0586	0.0529	0.0548

Notes: Ellipticity ratio: $\epsilon_{1001} = 0.5 \cdot [(O_2 \leftrightarrow O_6) + (O_2 \leftrightarrow O_2)] / (O_2 \leftrightarrow O_2)$; Mg-polyhedral volume (V_{polMg} , Å³) and polyhedral distortion coefficient (ξ , dimensionless) according to Balić-Zunić and Vickovic (1996) and Makovicky and Balić-Zunić (1998).

^a Crystal in the DAC without *P*-medium.

TABLE 5b. Selected bond distances (Å), ring “diameters” (Å) and other structural parameters of cordierite compressed in H₂O at different pressures

<i>P</i> (GPa)	0.0001	0.0001 ^a	0.39(6)	1.41(8)	1.75(5)
M-O ₁ (×2)	2.102(1)	2.100(5)	2.102(5)	2.089(6)	2.087(6)
M-O _{1,6} (×2)	2.110(1)	2.112(5)	2.105(5)	2.103(5)	2.106(5)
M-O ₃ (×2)	2.117(1)	2.115(6)	2.116(6)	2.110(6)	2.119(6)
<M-O>	2.110	2.109	2.108	2.101	2.104
T ₁ -O ₃ (×2)	1.757(1)	1.745(5)	1.751(5)	1.753(5)	1.742(6)
T ₁ -O ₁ (×2)	1.758(1)	1.756(6)	1.756(6)	1.749(6)	1.745(6)
<T ₁ -O>	1.7575	1.7505	1.7535	1.7510	1.7435
T _{1,6} -O ₆ (×4)	1.628(1)	1.626(4)	1.627(4)	1.624(4)	1.625(4)
T ₂ -O ₂	1.589(1)	1.586(7)	1.584(7)	1.588(7)	1.583(8)
T ₂ -O ₃	1.603(2)	1.592(8)	1.593(8)	1.582(8)	1.593(8)
T ₂ -O ₁ (×2)	1.637(1)	1.637(5)	1.633(5)	1.628(5)	1.626(5)
<T ₂ -O>	1.6165	1.6130	1.6108	1.6065	1.6070
T ₃ -O ₆	1.576(1)	1.575(6)	1.583(6)	1.586(7)	1.573(7)
T ₃ -O ₃	1.617(2)	1.612(8)	1.614(8)	1.606(8)	1.602(9)
T ₃ -O ₃ (×2)	1.638(1)	1.641(5)	1.632(5)	1.624(5)	1.627(5)
<T ₃ -O>	1.6173	1.6173	1.6152	1.6100	1.6073
T ₆ -O ₆	1.710(1)	1.715(6)	1.711(7)	1.707(7)	1.695(8)
T ₆ -O ₂	1.712(2)	1.709(7)	1.711(7)	1.708(7)	1.694(8)
T ₆ -O ₆ (×2)	1.775(1)	1.768(5)	1.768(5)	1.760(5)	1.766(4)
<T ₆ -O>	1.7430	1.7400	1.7395	1.7338	1.7303
O ₂ ↔ O ₃	5.837(2)	5.872(12)	5.846(14)	5.835(14)	5.861(17)
O ₆ ↔ O ₆	5.054(2)	5.038(20)	4.956(21)	4.937(21)	4.967(27)
O ₂ ↔ O ₂	5.521(2)	5.517(12)	5.503(15)	5.530(15)	5.527(17)
ε ₁₀₀₁	0.906(1)	0.899(4)	0.894(4)	0.897(4)	0.895(6)
T ₂ -O ₂ -T ₂	176.6(1)	176.8(6)	176.4(7)	177.4(7)	178.0(8)
T ₃ -O ₃ -T ₃	179.2(1)	177.8(7)	178.7(7)	178.7(8)	177.3(8)
T ₆ -O ₆ -T ₆	163.9(1)	164.1(5)	161.4(5)	161.4(5)	163.1(6)
O ₆ -O ₃ -O ₂	112.7(7)	111.9(5)	111.5(5)	111.7(5)	111.5(6)
O ₂ -O ₂ -O ₂	117.95(7)	118.2(4)	117.5(4)	116.9(5)	117.4(5)
O ₂ -O ₆ -O ₂	129.35(7)	129.8(3)	130.9(4)	131.4(4)	131.2(5)
V _{polMg}	11.80(1)	11.76(6)	11.75(7)	11.63(7)	11.66(8)
ξ	0.0578	0.0600	0.0580	0.0587	0.0617

^a Crystal in the DAC without *P*-medium.

which represent the equilibrium phase boundary between ice-VI and ice-VII (Chen and Yoo 2011, and references therein). Data points measured above this critical pressure boundary are characterized by increasing deviatoric stress as this is manifested through significant peak broadening of XRD Bragg peak profiles. For the given quality we did not regard these measurements as relevant. Compression in argon and methanol-ethanol mix was achieved within the quasihydrostatic regime as reported by Angel et al. (2007). Nevertheless, regardless of the use of fully hydrostatically acting pressure media, the intensities of Bragg reflections significantly dropped for all samples at $P \geq 6.9$ GPa, along with drastic peak broadening, together with changes in the peak profiles, which indicate metrical changes, the existence of more than one crystal domain, and structural gradients across domain boundary walls.

Apart from a minor shift of the P - V compression data in argon due to the small difference Mg/Fe ratio of the Tsi1 and Tsi2 samples, the three P - V data sets reveal almost identical compression behavior with no visible differences for $-dV/dP$. It appears that, within the experimental error of the measurements, all samples show identical volume dependencies being independent on the type of medium used for pressurization. The isothermal bulk moduli, $K_{0,298}$, for compression at room temperature (298 K) yield $K_{0,298} = 137.8 \pm 1.5$ GPa (in H₂O), 127.7 ± 2.3 GPa (in Ar) and 131.0 ± 1.3 GPa (in 4:1-ME) for a parametrized fit to the P - V data sets according to a third-order Birch-Murnaghan EoS (Angel 2000). These results reveal almost identical compressibility within the given standard deviations and considering

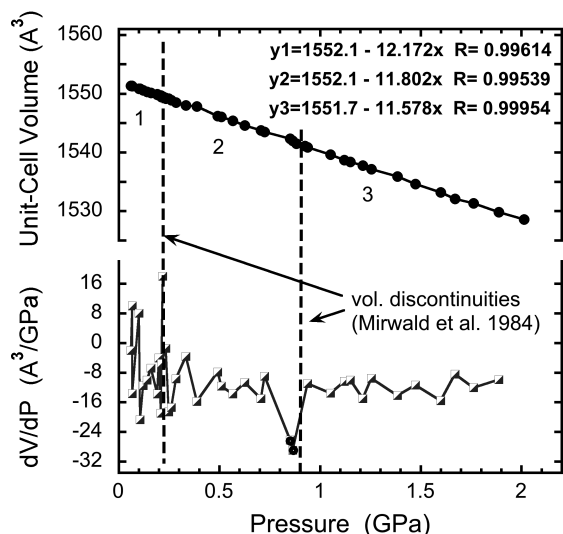


FIGURE 3. Cell volume (top) and compression coefficient dV/dP (bottom) obtained from cordierite (Tsi2_b#3) pressurized in DAC with water as pressure medium. The dV/dP data give a vague hint for irregularities at around 0.35 and 0.85 GPa, which is next to the supposed volume discontinuities previously reported. Linear fits to the volume data truncated to the three sections (1, 2, and 3) yield differences in the slope of about 2%.

correlation between K_0 and K' ($= dK/dP$) fit parameters. The pressure derivatives K' result in remarkable values of -6 ± 2 , $+0.4 \pm 0.9$, and -0.5 ± 0.4 , respectively, which corresponds to the apparent linear pressure dependency (Fig. 4). In this context, the larger value for the bulk modulus in water (~ 138 GPa) appears to correlate with the large negative value of dK/dP (-6 ± 2), as a fit with K' set 0 yields 132.1 ± 0.7 GPa for the bulk modulus. The bulk moduli obtained here are then similar to the values of 129(1) GPa (Toohill et al. 1999) and 129(2) GPa (Haussühl et al. 2011), considering them to be adiabatic bulk moduli as determined from Brillouin scattering and resonant ultrasound spectroscopy, respectively. In a similar fashion, the discrepancy of isothermal bulk modulus K_0 being only 115(1) GPa, as reported by Likhacheva et al. (2013), can be explained as a result of fitting the P - V data to a second-order Murnaghan EoS with fixing K' to 4. The re-evaluation of the data up to 4 GPa fitting K_0 with setting $K' = 0$ gives $K_0 = 127.6$ GPa for the bulk modulus, which is in perfect agreement with the results of this and earlier studies (Toohill et al. 1999; Haussühl et al. 2011). Comparison of all experimental data (Fig. 4) shows that, for compression at room temperature, the choice of pressurizing media is not critical. This certainly applies to a water-free methanol-ethanol mixture, but also to argon in the quasihydrostatic pressure regime up to 9 GPa. Using pure H₂O within the range of apparent hydrostaticity ($P < 2$ GPa), neither the equation of state nor structure refinements give evidence for a pressure-induced over-hydration. Although previous experimental studies at high P and T clearly showed that Ar and H₂O can be hosted by the cordierite structure (Schreyer et al. 1960; Schreyer and Yoder 1964; Armbruster 1985b), we find no evidence for interpenetration of excess Ar and H₂O within the

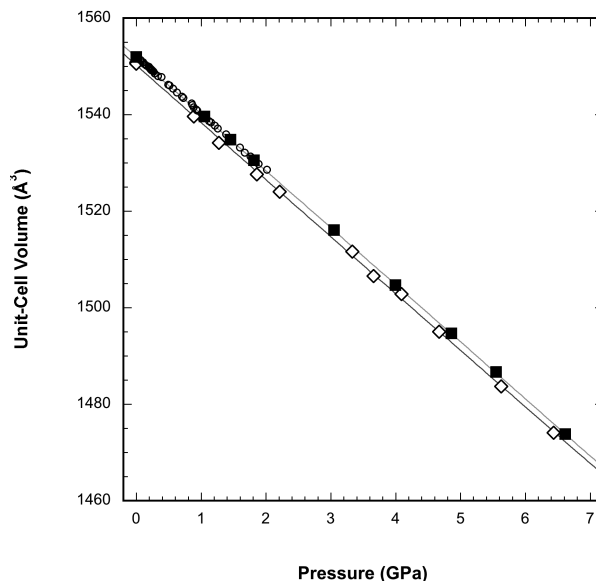


FIGURE 4. Unit-cell volumes from single-crystal XRD of cordierite in H₂O (open circles), in argon (open diamonds), and 4:1 methanol-ethanol (full squares). Lines correspond to the fit of a third-order Birch-Murnaghan EoS to the individual P - V data sets.

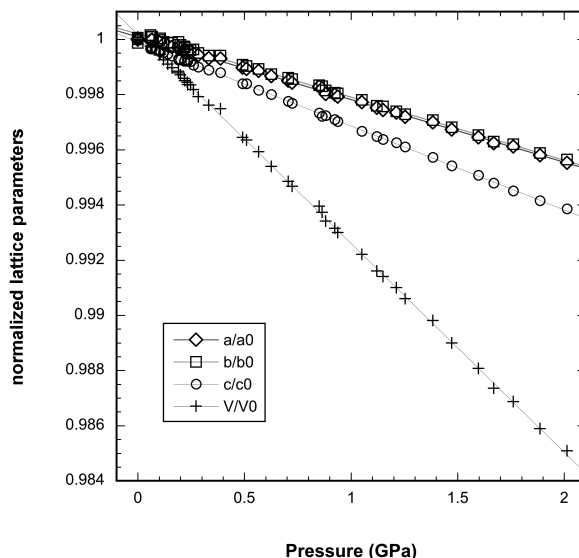


FIGURE 5. Lattice parameters a , b , c , and unit-cell volume V of cordierite in H₂O (in the hydrostatic pressure range 10^{-4} to 2.01 GPa). a/a_0 (open diamonds), b/b_0 (open squares), c/c_0 (open circles), and V/V_0 (crosses). Plotted lines correspond to linear fits with β_i^{-1} ($i = a, b, c$) = 440.0, 438.3, 328.7 GPa and $K_0 = 132.1$ GPa, respectively.

investigated pressure ranges up to 7 and 2 GPa, respectively, at room- T . This might be easily understood as we remained well below the critical pressure of over-hydration (above ~ 4 GPa; Likhacheva et al. 2013).

The evaluation of P - V data clearly suggests an elastic anomaly

obviously related to the observed structural change at ~ 6.9 GPa. The unusual linear compressibility is even confirmed by the compressibility data collected in H_2O with a high density of data points within a small pressure range between 10^{-4} and 2.01 GPa (Fig. 5). At first glance, the high-resolution P - V data sets, which correspond to individual measurements of the unit-cell volume with small pressure increments, do not reveal a discontinuity, neither in the volume nor for the individual axis directions. In particular, around 0.22 GPa the data suggest a smooth line with no indication for any changes in the slope (Fig. 5), i.e., neither a significant change of the bulk nor of the axial compressibilities. Plotting the calculated compressibility, i.e., as derived from ΔV and ΔP between neighboring data points (Fig. 3), the inspection of the almost linear appearance might give hints of possible irregularities at 0.35 and 0.85 GPa. The analysis of the unit-cell volume data suggests two to three sections, and linear fits to the volume data of the different sections yield very small differences for the slopes by ~ 2 – 3% . While the slope for the interval below 0.35 GPa is evolving in a positive fashion indicating slightly increasing stiffening, the evolution of bulk modulus for $P > 0.35$ GPa follows a constant line, which approximates $dK/dP = 0$. The deviation of two data points at 0.851 and 0.864 GPa (black in Fig. 3) might be considered as outliers within an applied 3 criteria for the given errors, and hence not being significant to prove a change in the compressional behavior related to the previously suspected discontinuity at ~ 0.85 GPa.

Anisotropy of compression and of the elastic softening

According to the hexagonal topology of polyhedral arrangement, which follows the beryl structure by ignoring the cation ordering on the T sites, the compressional anisotropy of the framework structure reveals similar compression for the a and b axis, both being less compressible than the c axis (Fig. 5). This behavior of the c -axis direction being comparably softer than the lattice directions perpendicular to the c axis has been reported for experimental investigations on beryl [$\beta_{\perp} = 1.72(4) \times 10^{-3} \text{ GPa}^{-1}$ and $\beta_{\parallel} = 2.10(9) \times 10^{-3} \text{ GPa}^{-1}$; Hazen et al. (1986)] but also for measured and calculated elastic moduli in beryl [$C_{11} = 306.3$ GPa, $C_{33} = 282.2$ GPa, Yoon and Newnham (1973); Prencipe et al. (2011)]. The behavior of similar compression of the a - and b -axis direction in cordierite (Table 6) corresponds rather to the expectations from symmetry aspects and is also confirmed

TABLE 6. Results of the fits for the pressure dependencies of the crystallographic axes and the Birch-Murnaghan equation of state

$V_0 (\text{\AA}^3);$ $a, b, c (\text{\AA})$	$K_{T=298},$ $\beta_i^{-1} (\text{GPa})$	$\partial K/\partial P,$ $\partial(\beta_i^{-1})/\partial P$	χ^2_w	$ P_{\text{obs}} - P_{\text{calc}} $ (GPa)
Cordierite in H_2O (10^{-4} to 2.01 GPa)				
$V_0 = 1551.83(3)$	$K_{T=298} = 137.8(1.5)$	$\partial K/\partial P = -6.4(1.8)$	1.35	≤ 0.011
$a_0 = 17.0732(2)$	$1/3 \beta_a^{-1} = 150.8(2.7)$	$1/3 \partial(\beta_a^{-1})/\partial P = -5.1(3.0)$	1.16	≤ 0.019
$b_0 = 9.7243(2)$	$1/3 \beta_b^{-1} = 146.8(4.4)$	$1/3 \partial(\beta_b^{-1})/\partial P = -2.3(4.9)$	2.31	≤ 0.051
$c_0 = 9.3483(2)$	$1/3 \beta_c^{-1} = 105.2(1.6)$	$1/3 \partial(\beta_c^{-1})/\partial P = 4.5(1.9)$	0.95	≤ 0.013
Cordierite in argon (10^{-4} to 6.44 GPa)				
$V_0 = 1550.56(15)$	$K_{T=298} = 127.7(2.3)$	$\partial K/\partial P = 0.4(0.9)$	3.54	≤ 0.026
$a_0 = 17.0728(7)$	$1/3 \beta_a^{-1} = 117.9(2.3)$	$1/3 \partial(\beta_a^{-1})/\partial P = 11.2(1.3)$	2.63	≤ 0.012
$b_0 = 9.7198(4)$	$1/3 \beta_b^{-1} = 148.1(2.8)$	$1/3 \partial(\beta_b^{-1})/\partial P = -4.3(0.9)$	1.04	≤ 0.053
$c_0 = 9.3437(6)$	$1/3 \beta_c^{-1} = 116.1(2.4)$	$1/3 \partial(\beta_c^{-1})/\partial P = -1.2(0.8)$	3.00	≤ 0.023
Cordierite in ethanol-methanol (10^{-4} to 6.61 GPa)				
$V_0 = 1551.97(15)$	$K_{T=298} = 131.0(1.3)$	$\partial K/\partial P = -0.5(0.4)$	0.83	≤ 0.008
$a_0 = 17.0722(8)$	$1/3 \beta_a^{-1} = 121.7(2.2)$	$1/3 \partial(\beta_a^{-1})/\partial P = 9.3(0.9)$	1.66	≤ 0.005
$b_0 = 9.726(6)$	$1/3 \beta_b^{-1} = 133.4(7.8)$	$1/3 \partial(\beta_b^{-1})/\partial P = -1.9(1.9)$	5.83	≤ 0.067
$c_0 = 9.348(2)$	$1/3 \beta_c^{-1} = 129.9(4.9)$	$1/3 \partial(\beta_c^{-1})/\partial P = -3.5(1.0)$	11.3	≤ 0.047

by the linear coefficients $\beta_a = \beta_b = 2.4(1) \times 10^{-3} \text{ GPa}^{-1}$ and $\beta_c = 3.1(1) \times 10^{-3} \text{ GPa}^{-1}$ in the pressure range below 3 GPa (Likhacheva et al. 2013). Nevertheless, the similar compression in an initial stage at moderate pressures starts to develop continuously into a diversification between the two axes at pressures greater than 3 to 4 GPa (Fig. 6). While the a axis gets the less compressible axis and shows conventional stiffening with pressure [i.e., $(\partial\beta_a^{-1})/\partial P$

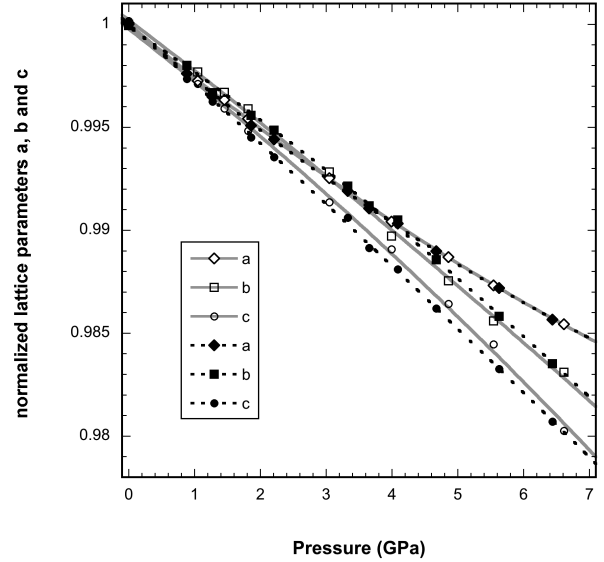


FIGURE 6. Lattice parameters a , b , and c of cordierite in methanol-ethanol mix (open symbols) and argon (full symbols). Plotted data correspond to normalized parameter a/a_0 (diamonds), b/b_0 (squares), c/c_0 (circles); lines correspond to fits of a Birch-Murnaghan EoS with axial moduli β_i^{-1} ($i = a, b, c$) and their pressure derivatives $\partial(\beta_i^{-1})/\partial P$ (see Table 6).

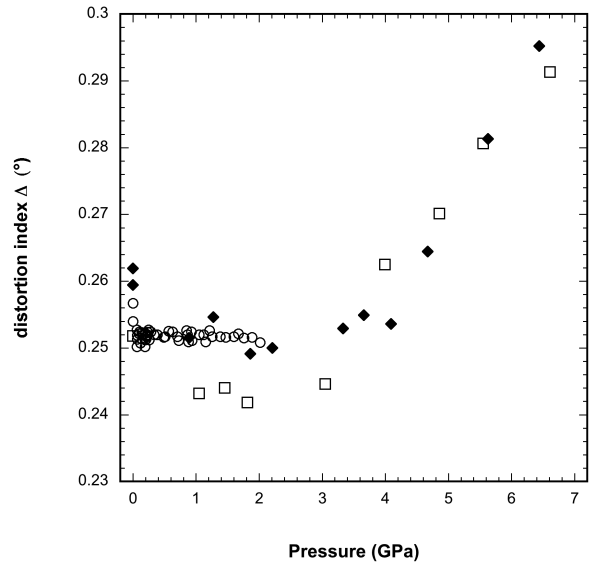


FIGURE 7. Evolution of the distortion index $\Delta (^{\circ}) = 1.094 (a - \sqrt{3}b)$ (Miyashiro 1957) with pressure for the data of cordierite compressed in H_2O (open circles), argon (full diamonds), and methanol-ethanol mixture (open squares). Note the significant change in the trend with starting to increase with pressure above ~ 4 GPa.

$= +11.2 \pm 1.3$ in argon and $+9.3 \pm 0.9$ in 4:1 methanol-ethanol mix], the b axis reveals anomalous behavior [i.e., $(\partial(\beta_b^{-1})/\partial P) = -4.3 \pm 0.9$ and -1.9 ± 1.9] and clearly indicates to be involved in elastic softening associated with an upcoming structural instability. In addition to the b axis, the c axis compression shows an analogous behavior with getting softer as expressed by the negative value for $\partial(\beta_c^{-1})/\partial P$ (see Table 6). The pronounced anisotropy within the ab plane is similar to the compressional anisotropy observed for the over-hydrated cordierite above 5 GPa (Likhacheva et al. 2013), where the a axis becomes the stiffest [$\beta_a = 1.6(1) \times 10^{-3} \text{ GPa}^{-1}$] in comparison to the b - and c -axis directions [$\beta_b = 2.7(1) \times 10^{-3} \text{ GPa}^{-1}$, $\beta_c = 3.0(1) \times 10^{-3} \text{ GPa}^{-1}$].

The diversification between the a and b axis is even more obvious when plotting the distortion index Δ (Putnis 1980b; Selkregg and Bloss 1980). Figure 7 shows rather constant evolutions for all

three individual data sets below 3 GPa, but a clear change of the trend with a positive slope above 4 GPa, which appears to be the same within the accuracy of the data for compression in Ar and methanol-ethanol mixture. The distortion index Δ , originally a measure for the deviation from hexagonality in 2θ for selected reflections (Miyashiro 1957), was found to reach maximum values of 0.31° (Armbruster and Bloss 1980), with the value for Δ decreasing with the incorporation of Na^+ , H_2O , and CO_2 into the structural channels (Schreyer et al. 1979; Armbruster and Bloss 1980; Selkregg and Bloss 1980). All values, determined here from the distortion with pressure, approach the reported maximum value but lie below 0.31° .

Summarizing these findings, the compressional behavior of the main axes yields an anisotropy following the beryl structure topology with $\beta_a^{-1} \approx \beta_b^{-1} > \beta_c^{-1}$ for an initial pressure regime

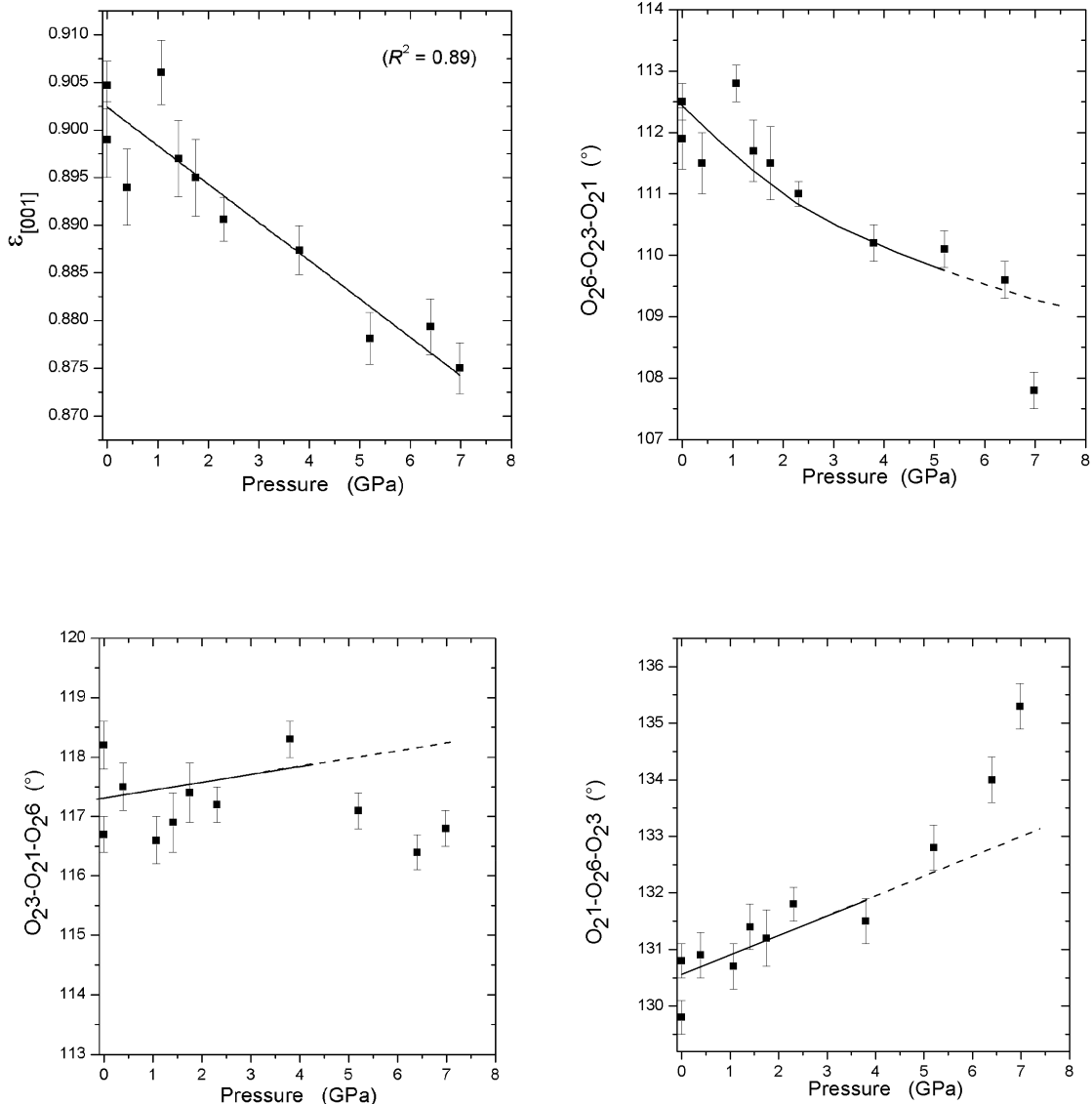


FIGURE 8. (a) Evolution of the ellipticity ratio of the 6-membered rings of tetrahedra running along [001] (i.e., $\epsilon_{[001]}$) and of the inter-tetrahedral angles (b) $\text{O}_{26}\text{-O}_{23}\text{-O}_{21}$, (c) $\text{O}_{23}\text{-O}_{21}\text{-O}_{26}$, and (d) $\text{O}_{21}\text{-O}_{26}\text{-O}_{23}$ ($^\circ$) with pressure. Lines represent the trends of evolution with pressure.

up to ~ 3 GPa. The compressional behavior of the a and b axis diversifies with increasing pressure and reveals increasing anisotropy of deformation within the ab plane, similar to the compressional anisotropy reported for the over-hydrated cordierite (Likhacheva et al. 2013). Both the increasing anisotropy and the bulk volume compression are characterized by remarkable elastic softening effects with significantly negative $\partial(\beta^{-1})/\partial P$ coefficients, in particular obtained for the compressibilities of the b - and c -axis directions.

Structure evolution up to 7 GPa

In response to the applied pressure, the structure of cordierite reacts mainly through inter-tetrahedral tilting, with oxygen atoms acting as flexible hinges, and through the polyhedral compression of the Mg-octahedron. The evolution of the tetrahedral bond distances (Table 5) shows only a subtle compression within the pressure range investigated, suggesting that the Si/Al-tetrahedra act as rigid units, whereas the inter-tetrahedral angles (i.e., $O_26-O_23-O_21$, $O_21-O_26-O_23$; Fig. 8; Table 5) change significantly. In particular, the angle $O_21-O_26-O_23$ tends to increase with P , whereas the angle $O_26-O_23-O_21$ decreases (Fig. 8; Table 5). Such mechanisms reflect the evolution of the ellipticity of the 6-membered rings of tetrahedra (6mR) perpendicular to $[001]$. The ellipticity ratio {here defined as $\epsilon_{[001]} = 0.5[(O_26 \leftrightarrow O_26) + (O_21 \leftrightarrow O_21)] / [(O_23 \leftrightarrow O_23)]$ } is 1 for an ideal undistorted ring (as expected for indialite) and a lower value indicates a higher ellipticity. Our structure refinements at high pressures show that $\epsilon_{[001]}$ is ~ 0.905 at ambient pressure and tends to decrease with P (Fig. 8; Table 5), reflecting an increase on the channel ellipticity as pressure increases. The increase of the ring ellipticity was postulated by Gatta and Lee (2006) and Gatta (2008) as an energetically less-costly mechanism, which somewhat accommodates the effect of pressure in open-framework materials. However, only a modest deformation of the $[001]$ -channel is observed within the P -range investigated (Fig. 8). While the data scatter in the low- P range does not reflect any clear deviation from linear trends, individual quantities (see Figs. 7 and 8) of the structures above 6 GPa might be interpreted as a precursor effect for the transformation at 6.9 GPa.

The high-pressure structure refinements show a significant compression of the Mg-polyhedron, as shown in Figure 9 and Table 5. The compressibility coefficient of the Mg-polyhedron, here derived by linear regression through the data points, is $\beta_{\text{poly}}(\text{MgO}_6) = 1.0(1) \times 10^{-2} \text{ GPa}^{-1}$, which leads to a polyhedral modulus of $K_{\text{poly}}(\text{MgO}_6) = 100(9) \text{ GPa}$. It is remarkable to point out that the Mg-polyhedron is, at a significant level, not deformed in response to the applied pressure, as shown by the evolution of the polyhedron distortion coefficient with P (ξ in Table 5). This somehow reflects the hexagonal topology of the cordierite framework, which controls the almost isotropic compression of the Mg-polyhedron.

The structure investigation under increasing H_2O pressure was mainly aimed to elucidate any potential pressure-induced over-hydration in cordierite, such as recently reported by Likhacheva et al. (2013). A careful inspection of the difference-Fourier maps of the electron density of the high- P refinements did not give any evidence for a pressure-driven penetration of molecules of the P -medium through the $[001]$ channel, as pre-

viously observed in other classes of open-framework materials compressed in hydrous media (Gatta 2008, 2010). In response to the modest applied $P(\text{H}_2\text{O})$ in this experiment ($P < 2$ GPa), as limited by the quasihydrostaticity of ice-VI before transforming to ice-VII at 2.1 GPa, the structure of cordierite does not show any significant deformation mechanism. The ellipticity ratio of the 6mR running along $[001]$ is constant within the e.s.d., and even the softest unit of the cordierite structure, represented by the Mg-octahedron, appears to be only marginally compressed. The structure refinements clearly suggest no pressure-induced changes related to the possible re-arrangement of H_2O molecules on extra-framework sites, which would have been indicative for over-hydration effects.

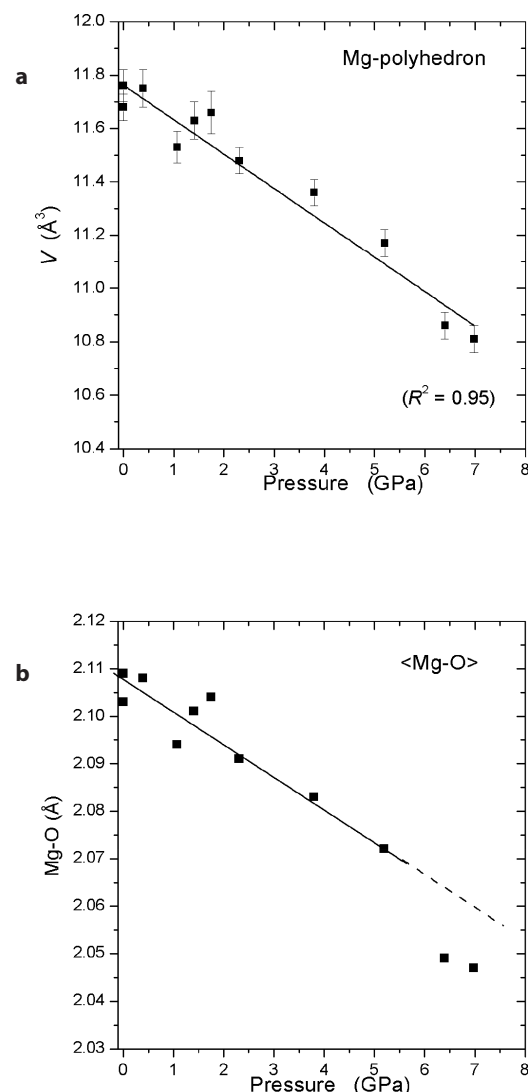


FIGURE 9. Evolution of (a) the polyhedral volume and (b) of the average $\langle \text{Mg-O} \rangle$ bond distances (see Table 5) of the Mg-octahedron with pressure. Lines represent the trends of evolution with P .

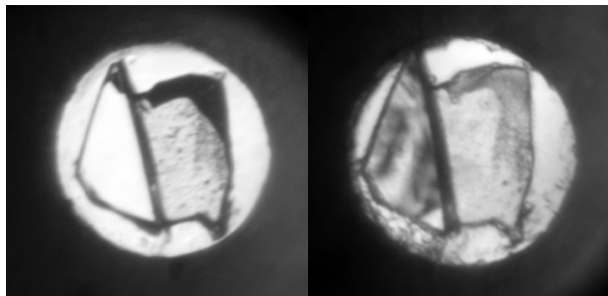


FIGURE 10. Cordierite single crystal (sample Tsi2_b#1, crystal on the left side) mounted together with quartz pressure standard (right side) below (~ 1.3 GPa) and above (~ 7.2 GPa) the transition at ~ 6.9 GPa (pressure medium: argon). Note the interference colors and gradual changes indicating strain across domain boundaries according to the orthorhombic-to-triclinic transition in comparison to the homogeneous single-domain crystal of orthorhombic symmetry at low pressure (image detail: $300 \times 300 \mu\text{m}$).

Changes of lattice metrics above 7 GPa

Any attempt to increase the pressure to values above ~ 7.0 GPa resulted in difficulties to center XRD peak profiles, which show significant broadening and did not allow to obtain any reliable high-precision data points for equation of state measurements. The optical inspection of the pressurized sample indicated inhomogeneities, the formation of domains, and optically visible strain across the sample crystals (Fig. 10). Using the strongest reflections of such a multi-domain crystal, the refinement of unit-cell parameters clearly indicated small but significant deviations from 90° of orthorhombic α , β , and γ angles. To overcome emerging strain in rather large crystals, tiny micrometer-sized sample crystals were chosen for investigations using synchrotron radiation. The sample loading of small crystal fragments provided almost unstrained single-domain crystals above the transition. The determined unit cell proves the orthorhombic-to-triclinic transition with consistent deviations from orthogonal lattice settings, in particular with the β angle around ~ 86.0 and the γ angle at 89.0 for base-vector settings corresponding to the orthorhombic C -centered unit cell at low pressures (Table 2). The lattice distortion appears to occur in a similar fashion such as reported for beryl, where the hexagonal structure undergoes a transition to a structure of triclinic symmetry above ~ 14 GPa (Prencipe et al. 2011). The unit-cell volume of cordierite here reveals a clear discontinuity across the critical transition pressure showing a spontaneous $\Delta V/V$ of approximately -6.9% as determined from unit-cell volumes measured at 7.53 and 9.0 GPa. The appearance of such a significant volume discontinuity associated with the transformation clearly suggests the structural transition to be first order in character. In this context, the pronounced anomaly of the compression behavior can be understood as elastic softening phenomenon typically associated with first-order transitions. The changes at the individual crystallographic axes follow the anisotropy observed for the compression of the orthorhombic polymorph. It is remarkable that the evolving anisotropy, as expressed by the different behavior between the a - and b -axis directions, leaves its trace even across the transition. A comparably large spontaneous shortening along the a -axis direction

from ~ 98.5 to $\sim 91.0\%$ of the original value is the most striking change associated with observed structural transformation. Any attempt to refine a triclinic structure model from the collected XRD intensity data sets did not yield yet a satisfying structure refinement of appropriate quality and will be reported elsewhere.

IMPLICATIONS

The experimental findings of this study allow improving the knowledge on the phase-stability and elastic behavior of cordierite. Up to date, the phase-diagram of cordierite was characterized by only two distinct fields, associated to Al_2Si -order/disorder phase transition with a low- T orthorhombic phase (C_{ccm} , at $T < 1750$ K, $P = 0.0001$ GPa) and a high- T hexagonal phase ($P6/mcc$, at $T > 1750$ K, $P = 0.0001$ GPa) (Miyashiro 1957; Langer and Schreyer 1969; Meagher and Gibbs 1977; Putnis 1980a; Armbruster 1985a; Redfern et al. 1989; Daniels et al. 1994; Malcherek et al. 2001). Our results lead to an enrichment of the phase-diagram with a new high- P triclinic polymorph at $P > 7$ GPa and $T = 293$ K. The orthorhombic-to-triclinic phase transition is governed by a volume contraction of about 7%. We still do not know the effect of temperature on the transition pressure, which will be investigated in the near future. In addition, the anomalous compressional pattern of the orthorhombic cordierite (with a negative bulk modulus P -derivative) has now a realistic explanation: it appears to be governed by the orthorhombic-to-triclinic transition. The results of this study are expected to improve the modeling of phase equilibria of petrological interest, as cordierite is a common mineral in medium- and high-grade pelitic metamorphic rocks or as porphyroblasts in hornfels found in contact metamorphic zones. Even in material sciences, where cordierite has received considerable attention for its pronounced stability at high temperatures, low thermal expansion, and an uncommon robust thermal shock resistance (Hochella et al. 1979; Mirwald 1981; Ikawa et al. 1986; Camerucci et al. 2001), our high-quality elastic data of the low- P polymorph and the P -induced densification in response to the orthorhombic-to-triclinic phase-transition would open a new scenario with further potential applications of this ceramic material.

ACKNOWLEDGMENTS

We thank Olaf Medenbach (Bochum) for the providing us crystal disks suitable for DACs, Herta Effenberger (Vienna) for performing the oscillation film photographs, Ilona Fin (Heidelberg) and Andreas Wagner (Vienna) for the sample preparation, Ilse Glass (Heidelberg) for EDX analyses, and Angela Ullrich, Pascal Schouwink, and Thomas Pippinger for their assistance in collecting individual EoS data points at Heidelberg. We thank Michael Hanfland (ESRF Grenoble) for his generous support on beamline ID09A. R.M. expresses his gratitude to the Laboratorium für Kristallographie, ETH Zürich, to have facilitated the use of equipment in the former high-pressure X-ray crystallography lab for the compressibility measurements in H_2O . T.L. is grateful to the European Research Council (ERC Starting Grant SULIWA) and the Austrian Science Fund (START award Y391) for financial support. Finally we thank Anna Likhacheva, Alexandra Friedrich, and one anonymous referee for their valuable suggestions, which significantly improved the manuscript.

REFERENCES CITED

- Abs-Wurmbach, I., Boberski, C., and Hafner, S. (1989) Zum Problem des Einbaus von dreiwertigem Eisen in den Cordierit: Synthesen und Mößbauerspektroskopie. *Fortschritte Mineralogie*, 66, 1.
- Agilent (2012) *CrysAlis Pro: User Manual*. Agilent Technologies, Yarnton, England.
- Angel, R.J. (2000) Equations of state. In R.M. Hazen and R.T. Downs, Eds., *High-temperature and high-pressure crystal chemistry*, 41, p. 35–60. Reviews in Mineralogy and Geochemistry, Mineralogical Society of America, Chantilly, Virginia.
- (2004) Absorption corrections for diamond-anvil pressure cells imple-

- mented in a software package Absorb-6.0. *Journal of Applied Crystallography*, 37, 486–492.
- Angel, R.J., and Finger, L.W. (2011) Single: A program to control single-crystal diffractometers. *Journal of Applied Crystallography*, 44, 247–251.
- Angel, R.J., Allan, D.R., Miletich, R., and Finger, L.W. (1997) The use of quartz as an internal pressure standard in high pressure crystallography. *Journal of Applied Crystallography*, 30, 461–466.
- Angel, R.J., Bujak, M., Zhao, J., Gatta, G.D., and Jacobsen, S.J. (2007) Effective hydrostatic limits of pressure media for high-pressure crystallographic studies. *Journal of Applied Crystallography*, 40, 26–32.
- Armbruster, T. (1985a) Crystal structure refinement, Si,Al-ordering, and twinning in “pseudo-hexagonal” Mg-cordierite. *Neues Jahrbuch Mineralogie, Monatshefte*, 1985, 255–267.
- (1985b) Ar, N₂, and CO₂ in the structural cavities of cordierite, and optical and X-ray single-crystal study. *Physics and Chemistry of Minerals*, 12, 233–245.
- (1986) Role of Na in the structure of low-cordierite: A single-crystal X-ray study. *American Mineralogist*, 71, 746–757.
- Armbruster, T., and Bloss, F.D. (1980) Channel CO₂ in cordierite. *Nature*, 286, 140–141.
- (1982) Orientation and effects of channel H₂O and CO₂ in cordierite. *American Mineralogist*, 67, 284–291.
- Balić-Žunić, T., and Vickovic, I. (1996) IVTON—a program for the calculation of geometrical aspects of crystal structures and some crystal chemical applications. *Journal of Applied Crystallography*, 29, 305–306.
- Bertoldi, C., Proyer, A., Garbe-Schönberg, D., Behrens, H., and Dachs, E. (2004) Comprehensive chemical analyses of natural cordierites: Implications for exchange mechanisms. *Lithos*, 78, 389–409.
- Birch, F. (1966) Compressibility, elastic constants. In S.P. Clark, Ed., *Handbook of physical constants*. Geological Society of America, Memoir, 97, 97–173.
- Bubeck, C. (2009) Direction dependent mechanical properties of extruded cordierite honey-combs. *Journal of European Ceramical Society*, 29, 3113–3119.
- Bulbak, T.A., Shvedenkov, G.Y., and Lepezin, G.G. (2002) On saturation of magnesian cordierite with alkanes at high temperatures and pressures. *Physics and Chemistry of Minerals*, 116, 140–154.
- Camerucci, M.A., Urretavizcaya, G., and Cavalieri, A.L. (2001) Mechanical behaviour of cordierite and cordierite-mullite materials evaluated by indentation techniques. *Journal of European Ceramic Society*, 21, 1195–1204.
- Chen, J.Y., and Yoo, C.S. (2011) High density amorphous ice at room temperature. *Proceedings of the National Academy of Sciences*, 108, 19, 7685–7688.
- Chervin, J.C., Canny, B., and Mancinelli, M. (2002) Ruby-spheres as pressure gauge for optically transparent high pressure cells. *High Pressure Research*, 21, 305–314.
- Cohen, J., Ross, F., and Gibbs, G.V. (1977) An X-ray and neutron diffraction study of hydrous low cordierite. *American Mineralogist*, 62, 67–78.
- Daniels, P., Wunder, B., Sahl, K., and Schreyer, W. (1994) Changing lattice metrics of synthetic cordierites: the metastable hexagonal to orthorhombic transformation sequence during isothermal annealing. *European Journal of Mineralogy*, 6, 323–335.
- Faye, G.H., Manning, P.G., and Nickel, E.H. (1968) The polarized optical absorption spectra of tourmaline, cordierite, chloritoid and vivianite: Ferric-ferrous electron interaction as a source of pleochroism. *American Mineralogist*, 53, 1174–1201.
- Förtsch, E., Uhr, W., and Wondratschek, H. (1992) A novel application of the spindle stage. *Microscope*, 40, 31–36.
- Gatta, G.D. (2008) Does porous mean soft? On the elastic behaviour and structural evolution of zeolites under pressure. *Zeitschrift für Kristallographie*, 223, 160–170.
- (2010) Microporous materials at high pressure: Are they really soft? In E. Boldyreva and P. Dera, Eds., *High-pressure crystallography: From Fundamental phenomena to technological applications*, p. 481–491. NATO Science for Peace and Security-Series B (Physics and Biophysics), Springer, DOI: 10.1007/978-90-481-9258-8_39.
- Gatta, G.D., and Lee, Y. (2006) On the elastic behavior of zeolite mordenite. A synchrotron powder diffraction study. *Physics and Chemistry of Minerals*, 32, 726–732.
- Geiger, C.A., Rager, H., and Czank, M. (2000a) Cordierite: III. The site occupation and concentration of Fe³⁺. *Contributions in Mineralogy and Petrology*, 140, 344–352.
- Geiger, C.A., Armbruster, T., Khomenko, V., and Quartieri, S. (2000b) Cordierite: I. The coordination of Fe²⁺. *American Mineralogist*, 85, 1255–1264.
- Goldman, D.S., and Rossman, G.R. (1977) Channel constituents in cordierite. *American Mineralogist*, 62, 1144–1157.
- Hausühl, E., Vinograd, V.L., Krenzel, T.F., Schreuer, J., Wilson, D.J., and Ottinger, J. (2011) High temperature elastic properties of Mg-cordierite: Experimental studies and atomistic simulations. *Zeitschrift für Kristallographie*, 226, 236–253.
- Hazen, R.M., Au, A.Y., and Finger, L.W. (1986) High pressure crystal chemistry of beryl (Be₃Al₂Si₆O₁₈) and euclase (BeAlSiO₄OH). *American Mineralogist*, 71, 977–984.
- Hejny, C., Miletich, R., Jasser, A., Schouwink, P., Crichton, W., and Kahlenberg, V. (2012) Second order *P6c2-P31c* structural transition and structural crystallography of the cyclosilicate benitoite, BaTiSi₃O₈, at high pressure. *American Mineralogist*, 97, 1747–1763.
- Hochella, M., Brown, G., Ross, F., and Gibbs, G. (1979) High temperature crystal chemistry of hydrous Mg- and Fe-cordierites. *American Mineralogist*, 64, 337–351.
- Ikawa, H., Otagiri, T., Imai, O., Suzuki, M., Urabe, K., and Udagawa, S. (1986) Crystal structures and mechanism of thermal expansion of high cordierite and its solid solutions. *Journal of the American Ceramic Society*, 69, 492–498.
- Khomenko, V.M., Langer, K., and Geiger, C.A. (2001) Structural locations of the iron ions in cordierite: a spectroscopic study. *Contributions in Mineralogy and Petrology*, 141, 381–396.
- King, H.E., and Finger, L.W. (1979) Diffracted beam crystal centering and its application to high-pressure crystallography. *Journal of Applied Crystallography*, 12, 374–378.
- Koepke, J., and Schulz, H. (1986) Single crystal structure investigation under high pressure of the mineral cordierite with an improved high-pressure cell. *Physics and Chemistry of Minerals*, 13, 165–173.
- Krauss, G., Reifler, H., and Steurer, W. (2005) Conically shaped single-crystalline diamond backing plates for a diamond anvil cell. *Review in Scientific Instruments*, 76, 105104, 1–5.
- Langer, K., and Schreyer, W. (1969) Infrared and powder X-ray diffraction studies of the polymorphism of cordierite. *American Mineralogist*, 54, 1442–1459.
- Le Breton, N., and Schreyer, W. (1993) Experimental CO₂ incorporation into Mg-cordierite: Nonlinear behaviour of the system. *European Journal of Mineralogy*, 5, 427–438.
- Likhacheva, A.Yu, Goryainov, S.V., Krylov, A.S., Bul’bak, T.A., and Prasad, P.S.R. (2011) Raman spectroscopy of natural cordierite at high water pressure up to 5 GPa. *Journal of Raman spectroscopy*, 43, 559–563.
- Likhacheva, A.Yu, Goryainov, S.V., and Bul’bak, T.A. (2013) An X-ray diffraction study of the pressure-induced hydration in cordierite at 4–5 GPa. *American Mineralogist*, 98, 181–186.
- Makovicky, E., and Balić-Žunić, T. (1998) New Measure of distortion for coordination polyhedra. *Acta Crystallographica B*, 54, 766–773.
- Malcherek, T., Domeneghetti, M.C., Tazzoli, V., Ottolini, L., McCammon, C., and Carpenter, M.A. (2001) Structural properties of ferromagnesian cordierites. *American Mineralogist*, 86, 66–79.
- Mao, H.K., Xu, J., and Bell, P.M. (1986) Calibration of the ruby pressure scale to 800 kbars under quasihydrostatic conditions. *Journal of Geophysical Research*, 9, 4673–4676.
- Meagher, E.P., and Gibbs, G.V. (1977) The polymorphism of cordierite: II. The crystal structure of indialite. *Canadian Mineralogist*, 15, 43–49.
- Medenbach, O., Maresch, W.V., Mirwald, P.W., and Schreyer, W. (1980) Variation of refractive index of synthetic Mg-cordierite with H₂O content. *American Mineralogist*, 65, 367–373.
- Miletich, R., Allan, D.R., and Kuhs, W.F. (2000) High-pressure single-crystal techniques. In R.M. Hazen and R.T. Downs, Eds., *High-temperature and high-pressure crystal chemistry*, 41, p. 445–520. *Reviews in Mineralogy and Geochemistry*, Mineralogical Society of America, Chantilly, Virginia.
- Miletich, R., Hejny, C., Krauss, G., and Ullrich, A. (2005) Diffraction techniques: Shedding light on structural changes. In R. Miletich, Ed., *Mineral Behaviour at Extreme Conditions*, 7, p. 281–338. EMU Notes, Eötvös University Press, Budapest.
- Miletich, R., Gatta, G.D., Redhammer, G.J., Burchard, M., Meyer, H.P., Weikusat, C., Rotiroti, N., Glasmacher, U.A., Trautmann, C., and Neumann, R. (2010) Structure alterations in microporous (Mg,Fe)₂Al₄Si₆O₁₈ crystals induced by energetic heavy-ion irradiation. *Journal of Solid State Chemistry*, 183, 2372–2381.
- Mirwald, P.W. (1981) Thermal expansion of anhydrous Mg-cordierite between 25 and 900 °C. *Physics and Chemistry of Minerals*, 7, 268–270.
- (1982) A high-pressure phase transition in cordierite. *American Mineralogist*, 67, 277–283.
- (2005a) The fine-structure of the dehydration boundary of brucite (Mg(OH)₂) up to 2.5 GPa – Indications of not-smooth PVT behaviour of supercritical H₂O. *European Journal of Mineralogy*, 17, 537–542.
- (2005b) Evidence of anomaly boundaries of water at high pressure from compression and NaCl*2H₂O dehydration experiments. *Journal of Chemical Physics*, 123, 124715.
- (2008) Experimental study of the dehydration reactions gypsum-bassanite and bassanite-anhydrite at high pressure: Indication of anomalous behaviour of H₂O at high pressure in the temperature range of 50–300 °C. *Journal of Chemical Physics*, 128, 074502.
- Mirwald, P.W., and Maresch, W.V. (1980) Ein Hochdruckphasenübergang in Cordierit. *Naturwissenschaften*, 67, 253–254.
- Mirwald, P.W., and Massonne, H.J. (1980) The low-high quartz and quartz-coesite transition to 40 kbar between 600 and 1600 °C and some reconnaissance data on the effect of NaAlO₂ component on the low quartz-coesite transition. *Journal of Geophysical Research*, B, 85, 6983–6990.
- Mirwald, P.W., Malinowski, M., and Schulz, H. (1984) Isothermal compression of low-cordierite to 30 kbar (25 °C). *Physics and Chemistry of Minerals*, 11,

- 140–148.
- Miyashiro, A. (1957) Cordierite-indialite relations. *American Journal of Science*, 255, 43–62.
- Nasdala, L., Wildner, M., Wirth, R., Groschopf, N., Pal, D.C., and Möller, A. (2006) Alpha particle haloes in chlorite and cordierite. *Mineralogy and Petrology*, 86, 1–27.
- Periotto, B., Nestola, F., Balić-Žunić, T., Angel, R.J., Miletich, R., and Olsen, L.A. (2011) Comparison between beryllium and diamond backing plates diamond anvil cells: Application to single-crystal X-ray diffraction high-pressure data. *Review in Scientific Instruments*, 82, 055111.
- Prencipe, M., Scanavino, I., Nestola, F., Merlini, M., Civalleri, B., Bruno, M., and Dovesi, R. (2011) High-pressure thermo-elastic properties of beryl ($\text{Al}_2\text{Be}_6\text{Si}_{12}\text{O}_{36}$) from ab initio calculations, and observations about the source of thermal expansion. *Physics and Chemistry of Minerals*, 38, 223–239.
- Putnis, A. (1980a) Order-modulated structures and the thermodynamics of cordierite reactions. *Nature*, 287, 128–131.
- (1980b) The distortion index in anhydrous Mg cordierite. *Contributions in Mineralogy and Petrology*, 74, 135–141.
- Redfern, S.A.T., Salje, E.K.H., Maresch, W., and Schreyer, W. (1989) X-ray powder diffraction and infrared study of the hexagonal to orthorhombic phase transition in K-bearing cordierite. *American Mineralogist*, 74, 1293–1299.
- Salzmann, C., Loerting, Th., Klotz, S., Mirwald, P.W., Hallbrucker, A., and Mayer, E. (2006) Isobaric annealing of high-density amorphous ice between 0.3 and 1.9 GPa: In situ values and structural changes. *Physical Chemistry Chemical Physics*, 8, 386–397.
- Schreyer, W., and Yoder, H.S. Jr. (1964) The system Mg-cordierite- H_2O and related rocks. *Neues Jahrbuch für Mineralogie, Abhandlungen*, 101, 271–342.
- Schreyer, W., Yoder, H.S. Jr., and Aldrich, L.T. (1960) Synthesis of argon-containing cordierite. *Annual Report of the Geophysical Laboratory 1959–1960*. Carnegie Institute of Washington Year Book, 59, 94–96.
- Schreyer, W., Gordillo, C.E., and Werding, G. (1979) A new sodian-beryllian cordierite from Soto, Argentina, and the relationship between distortion index, Be content, and state of hydration. *Contributions Mineralogy Petrology*, 70, 421–428.
- Selkregg, K.R., and Bloss, F.D. (1980) Cordierites: compositional controls of Δ , cell parameters, and optical properties. *American Mineralogist*, 65, 522–533.
- Sheldrick, G.M. (1997) SHELXS-97. Program for the solution of crystal structures. University of Göttingen, Germany.
- Toohill, K., Siegesmund, S., and Bass, J.D. (1999) Sound velocities and elasticity of cordierite and implications for deep crustal seismic anisotropy. *Physics and Chemistry of Minerals*, 26, 333–343.
- Vance, E.R., and Price, D.C. (1984) Heating and radiation effects on the optical and Mössbauer spectra of Fe-bearing cordierites. *Physics and Chemistry of Minerals*, 10, 200–208.
- Vry, J.K., Brown, P., and Valley, J. (1990) Cordierite volatile content and the role of CO_2 in high-grade metamorphism. *American Mineralogist*, 75, 71–88.
- Weikusat, C., Glasmacher, U.A., Miletich, R., Neumann, R., and Trautmann, C. (2008) Raman spectroscopy of heavy ion induced damage in cordierite. *Nuclear Instruments and Methods in Physical Research B*, 266, 2990–2993.
- Weikusat, C., Miletich, R., Glasmacher, U.A., Trautmann, C., and Neumann, R. (2010) Heavy ion irradiation on crystallographically oriented cordierite and the conversion of molecular CO_2 to CO —A Raman spectroscopic study. *Physics and Chemistry of Minerals*, 37, 417–424.
- Wilson, A.J.C., and Prince, E. (1999) *International Tables for Crystallography, Volume C, Mathematical, physical and chemical tables* (third edition), 578 p. Kluwer, Dordrecht.
- Yoon, H.S., and Newnham, R.E. (1973) The elastic properties of beryl. *Acta Crystallographica*, A29, 507–509.

MANUSCRIPT RECEIVED JANUARY 30, 2013

MANUSCRIPT ACCEPTED NOVEMBER 15, 2013

MANUSCRIPT HANDLED BY ALEXANDRA FRIEDRICH